JOURNAL OF GEOPHYSICAL RESEARCH, VOL. 116, B02403, doi:10.1029/2010JB007607, 2011

On-land ice loss and glacial isostatic adjustment at the Drake Passage: 2003–2009

Erik R. Ivins,[1] Michael M. Watkins,[1] Dah-Ning Yuan,[1] Reinhard Dietrich,[2]
Gino Casassa,[3] and Axel Rülke[4]

Received 29 March 2010; revised 16 September 2010; accepted 4 November 2010; published 8 February 2011.

[1] Land glacier extent and volume at the northern and southern margins of the Drake Passage have been in a state of dramatic demise since the early 1990s. Here time-varying space gravity observations from the Gravity Recovery and Climate Experiment (GRACE) are combined with Global Positioning System (GPS) bedrock uplift data to simultaneously solve for ice loss and for solid Earth glacial isostatic adjustment (GIA) to Little Ice Age (LIA) cryospheric loading. The present-day ice loss rates are determined to be −26 ± 6 Gt/yr and −41.5 ± 9 Gt/yr in the Southern and Northern Patagonia Ice Fields (NPI+SPI) and Antarctic Peninsula (AP), respectively. These are consistent with estimates based upon thickness and flux changes. Bounds are recovered for elastic lithosphere thicknesses of $35 \leq h \leq 70$ km and $20 \leq h \leq 45$ km and for upper mantle viscosities of $4–8 \times 10^{18}$ Pa s and $3–10 \times 10^{19}$ Pa s (using a half-space approximation) for NPI+SPI and AP, respectively, using an iterative forward model strategy. Antarctic Peninsula ice models with a prolonged LIA, extending to A.D. 1930, are favored in all χ^2 fits to the GPS uplift data. This result is largely decoupled from Earth structure assumptions. The GIA corrections account for roughly 20–60% of the space-determined secular gravity change. Collectively, the on-land ice losses correspond to volume increases of the oceans equivalent to 0.19 ± 0.045 mm/yr of sea level rise for the last 15 years.

Citation: Ivins, E. R., M. M. Watkins, D.-N. Yuan, R. Dietrich, G. Casassa, and A. Rülke (2011), On-land ice loss and glacial isostatic adjustment at the Drake Passage: 2003–2009, *J. Geophys. Res.*, *116*, B02403, doi:10.1029/2010JB007607.

1. Introduction

[2] The demise of glacier mass along the coastal corridor of the southernmost Cordilleran mountains is attributed to regional and well-documented climate warming sustained since at least 1930 in the Antarctic Peninsula and 1870 in southern Patagonia [e.g., *Masiokas et al.*, 2009; *Hall*, 2009; *Thompson et al.*, 1994; *Mayewski et al.*, 2009; *Thomas et al.*, 2009]. Measurements of thickness change and ice flux velocity provide much of the critical information from 1990–2003, a time over which ice losses accelerated [*Rignot et al.*, 2003; *Pritchard and Vaughan*, 2007; *Rignot et al.*, 2008]. Here we use mascon solutions of the ranging data between the GRACE satellite pair and high-precision bedrock uplift data to derive a 6.25 year trend in total mass as the satellites pass over the SPI + NPI and Graham Land (GL) of the Antarctic Peninsula (AP) during January 2003 to March 2009. Recent climate changes in the southern hemisphere have been attributed to a strengthening of the circumpolar westerly winds that encircle the Antarctic continental ice sheet [*Thompson and Solomon*, 2002; *Vaughan et al.*, 2003]. The net effect of this strengthening is to drive cooler summer temperatures in coastal east Antarctica and warmer temperatures in coastal lands both south and north of the Drake Passage by −1.5 ± 0.5°C and +3.5 ± 0.5°C, respectively, over the past 50 years [*Thompson and Solomon*, 2002; *Turner et al.*, 2005; *van Lipzig et al.*, 2008; *Mayewski et al.*, 2009]. Southernmost South American summer atmospheric temperature trends during the past 100 years exceed +2.5°C in the latitude range of 45–58°S [*Jones et al.*, 1999].

[3] The mass balances of marine and freshwater outlet glaciers are negatively affected by this warming: to the south the AP glaciers have lost floating frontal ice in nine ice shelf breakup events since 1989. This ice supplies a stabilizing buttress force at the grounding line. Adjacent to the Drake Passage, at least 200 tidewater glaciers have been experiencing accelerated losses measured from 1993 to 2003 by nongravitational methods [*Rignot et al.*, 2003; *Pritchard and Vaughan*, 2007; *Rignot et al.*, 2008]. During the last 15 years glaciers that drain the Bruce Plateau (BP) and the Patagonian Ice Fields (PIF) (Figure 1, top and bottom inserts, respectively) are losing mass per unit area at some of the most intense rates found on Earth. High-resolution atmospheric simulations indicate that intensification of surface tempera-

---

[1] Jet Propulsion Laboratory, California Institute of Technology, Pasadena, California, USA.

[2] Institut für Planetare Geodäsie, Technische Universität Dresden, Dresden, Germany.

[3] Centro de Estudios Científicos, Valdivia, Chile.

[4] Bundesamt für Kartographie und Geodäsie, Leipzig, Germany.

0148-0227/11/2010JB007607

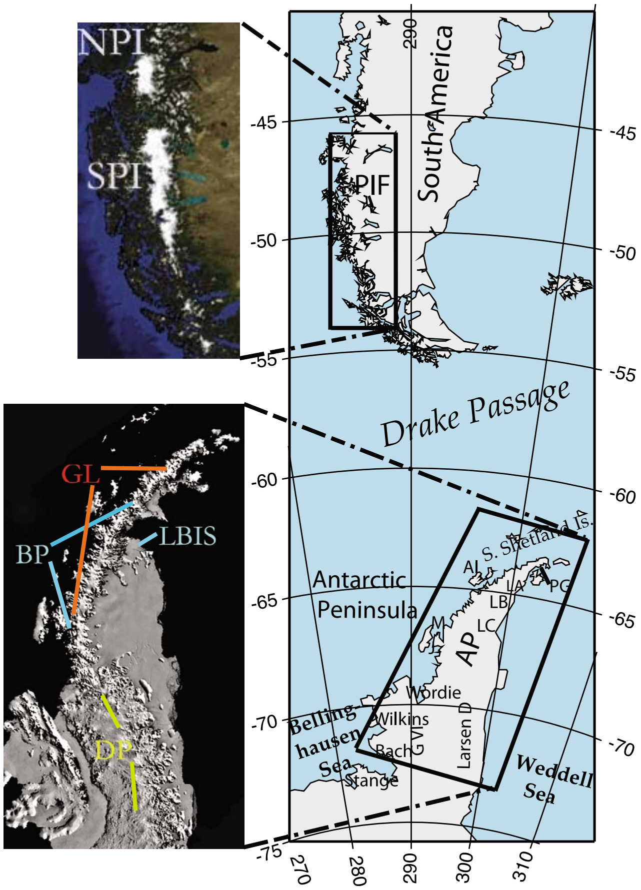

Figure 1. Location map of the Patagonian Ice Fields (PIF) (SPI+NPI) and Antarctic Peninsula (AP). The major ice shelves [*Cook and Vaughan*, 2010] relevant to our ice load models and the location of Anvers Island (AI) are indicated. (Abbreviated ice shelf names are LA, Larsen A; LB, Larsen B; LC, Larsen C; PG, Prince Gustav; M, Müller; and J, Jones.) The top left insert shows the locations of the Northern (NPI) and Southern Patagonian Ice Fields (SPI). The bottom left insert shows the extent of Graham Land (GL), Bruce Plateau (BP), and Dyer Plateau (DP). The location of the partially disintegrated Larsen B Ice Shelf (LBIS) is also shown.

ture during the late summer melt season promoted the dramatic disintegration of Larsen B Ice Shelf (LBIS) in 2002 just east of the BP in the AP [*van Lipzig et al.*, 2008].

[4] An important question is to decipher whether or not the trend toward increased glacier mass losses in the AP and SPI+NPI are representative of transient interannual variability, of further pronounced acceleration, or of a transition into a longer-term climate mode that will lead to a new configuration of the on-land cryosphere that radically departs from the present one. New GRACE data that allow continuity with past mass change measurements therefore bear heavily on answering this question. GRACE provides an especially potent data set to answer this question because they do not require independent and coeval measurements of both the surface mass balance components and glacial fluxes. Annual rates of snow accumulation and glacier outflux may both be changing in the AP, and there may be particularly large uncertainty in the rate at which precipitation varies. One of the most important challenges faced by glaciologists is to simultaneously capture, in as complete a record as possible, all positive and negative parts of the mass balance. While GRACE is ideally suited to such a challenge, often it must be corrected for a poorly determined GIA signal. Here we report mass trends in water height equivalent (WHE) change determined with a relatively new GRACE global mascon treatment (GLM), providing superior spatial resolution. Most importantly, we couple the space gravity and vertical GPS station position data in order to simultaneously solve for GIA and a 6.25 year trend in on-land cryospheric mass change. GRACE mass balance studies in Antarctica and Patagonia have been hampered by large uncertainties in the GIA correction. For Antarctica the correction can dominate the amplitude of solutions for trend in ice mass [*Velicogna and Wahr*, 2006; *Chen et al.*, 2008, 2009]. The correction also offers a large uncertainty in the Patagonian Ice Fields [*Chen et al.*, 2007]. While space gravimetry can uniquely determine mass change confined to the surface of the Earth, it cannot do so for mass variability in three dimensions, even with the most ideal suppression of observational error [*Chao*, 2005]. This nonuniqueness highlights the crucial role of GPS-determined crustal motion data for placing improved bounds on the GIA corrections, as the later involve flow in the deep Earth.

[5] The method in this paper is to use the GPS data to constrain competing GIA models. We test for viable a priori ice evolution scenarios with extensive forward model and back-stepping parameter corrective updates. The tests define nonunique classes of ice-Earth parameter models that satisfy known evolutionary constraints and independent present-day loss estimates. For the peninsula, three classes of models compete in the quality of their predictions of the uplift data. Viable models must also be compatible with both the amplitude and spatial character of the observed GRACE trend fields, although each will give slightly different GIA corrections. An interesting feature of the end-product model solutions is that they can be used to infer ice height change, allowing comparison to ICESat (Ice, Cloud and Land Elevation Satellite) altimetric data taken during the GRACE-GPS observing period.

2. Global Mascon and GPS Trends

2.1. Spherical Cap Mascon Method for GRACE

[6] At the Jet Propulsion Laboratory (JPL) a spherical cap mascon method for analysis of the accelerations on the two satellites has been developed from first principles using direct integration of the perturbative spatial variations expressed as planetary surface mass elements. The traditional orbit analysis of gravity uses a spherical harmonic formalism, such as that developed by *Kaula* [1966]. However, alternative direct analytical techniques have been in use for many years [e.g., *Pick*, 1984; *Tenzer et al.*, 2007]. An independently derived analytic method for a spherical, axisymmteric surface cap has been modeled into the JPL MIRAGE software [*Guinn et al.*, 1994] to calculate the gravitational force acting on the two spacecraft following a formulation described by *Sunseri* [2010]. This mascon formulation provides a native basis function for the estimated gravity solution, and avoids any intermediate expansion of the mascons in spherical

harmonics. The MIRAGE software models and filter parameterizations are generally derived from space navigation software systems at JPL, and as such are independent of those used at, for example, GeoForschungZentrum (GFZ) in Potsdam, the Center for Space Research (CSR) of the University of Texas at Austin or the other centers distributing GRACE solutions. For validation, the MIRAGE software and the CSR analysis software packages have been carefully intercompared for both the TOPEX/Poseidon project and for GRACE, when identical models and parameterizations are deliberately utilized. The parametrization and modeling used in the JPL GRACE analysis has been described by *Watkins and Yuan* [2007]. Although this implementation incorporates independent analysis procedures, we use the same geophysical dealiasing models as the CSR and GFZ analysis centers [e.g., *Flechtner et al.*, 2010]. By implementing a global mascon solution for each month of GPS orbital tracking and intersatellite range data a solution emerges each month that does not require destriping filters, a method critical for the highest resolution spherical harmonic fields [e.g., *Chen et al.*, 2007]. At Goddard Space Flight Center (GSFC) a new global formalism for GRACE mascon solutions has also been realized very recently [*Sabaka et al.*, 2010].

2.1.1. KBRA to Mascon and to Spherical Harmonic Fields

[7] Spherical harmonic (SH) fields have the utility that they can employ other models generated in the SH domain, such as Love numbers for solid and ocean tides, and also because geophysical applications of GRACE usually employ an isotropic Gauss filtering [*Wahr et al.*, 1998]. The solution employed here utilizes global 2-degree radii spherical cap mascons, solved for simultaneously with the satellite orbits and instrument parameters, using the direct partial derivatives of surface mass with respect to satellite-satellite range acceleration.

2.1.2. Mascon Resolution and a Down-Scaling Technique

[8] A regional mascon treatment (RMT) of rapid glacier change was given for the Gulf of Alaska [*Luthcke et al.*, 2008] where a well-constrained GIA was available [*Larsen et al.*, 2005]. The resolution using this RMT is impressive, with the half-wavelength resolution being $\Delta\lambda \approx 215$ km, or roughly $\Delta\lambda \approx R_E\,\pi/L$ (R_E is the mean radius of the Earth). The maximum order and degree of the corresponding mascon SH field is, in theory, M, L ≈ 96. The new GLM uses caps (mascons) of radii 222.6 km, thus having a theoretical resolving power, $\Delta\lambda$, comparable to RMT, while being global. All SH solution products distributed by the various analysis centers come with the caveat that time-varying gravity fields are resolved out to degree L ≈ 50, or resolving power $\Delta\lambda \cong 400$ km [*Wahr et al.*, 1998]. Another advantage of the GLM is the avoidance of problems with correlated errors at degree and orders $L \geq 11$. Notably, GLM does not employ an SH basis function in direct analysis of K-band range data, thus avoiding correlated error associated with orbital and nuisance parameter estimation. Additionally, the higher resolution provides strong mitigation of "leakage" errors, wherein signals from one, or more, nearby geophysical regions artificially appear in targeted regions of interest. While a host of filters have been proposed to diagnose and treat correlation and sampling errors [*Swenson and Wahr*, 2006; *Chambers*, 2006; *Horwath and Dietrich*, 2009] in the various releases of the SH fields, these treatments have a tendency to remove both error and real geophysical signal, particularly when the area is elongate north–south, as is the case with both SPI+NPI and GL. In spite of this difficulty, SH solution products have been used to address ice loss from SPI+NPI and GL [*Velicogna and Wahr*, 2006; *Chen et al.*, 2008; *Horwath and Dietrich*, 2009], but at quite low resolution, since the width of the target areas are 35–60 km.

2.1.3. Dual Ensembles: Mascons and Glacier-Specific Caps

[9] A glacier-specific ensemble of caps are defined that are of much smaller dimension than are the global mascons solved for by the analysis of orbits and range acceleration data. For example, in the case of Patagonia, caps correspond to the areal extents and locations of the measured glaciers for NPI and SPI as given in the supplementary tables of *Dietrich et al.* [2010]. These spatially distinct small ensemble caps (SCE) (see Figure 2 for Antarctic Peninsula distribution) model both the viscoelastically loaded Earth and represent the finite sources of surface mass changes that are the targets of secular, on-land, cryospheric mass variability. Both the glacier ensemble and the global mascon determined, global time-varying surface water mass fields are expanded into SH. Additionally, the solid Earth components of the glacial isostatic response to the glacier-specific caps may also be expanded in SH. This forms a common basis function and predictions from both glacier-specific and mascon-specific gravity acceleration perturbations can be mapped into to the nontidal time-varying external gravitational potential of the Earth:

$$\mathcal{T}(r,\theta,\lambda,t) = \frac{GM}{r}\sum_{\ell=1}^{L}\sum_{m=0}^{\ell}\sum_{j=1}^{2}\left\{\frac{R_E}{r}\right\}^{\ell}\overline{C}_{\ell mj}(t)\overline{Y}_{\ell mj}(\theta,\lambda), \qquad (1)$$

where r, θ, λ, t are radial position, colatitude, longitude and time, respectively, and GM is the product of the universal gravitational constant and planetary mass. The Earth's mean surface gravity is g and mean radius is R_E. Here $\overline{Y}_{\ell mj}$ are normalized real surface harmonics [*James and Ivins*, 1998; *Wahr et al.*, 1998] and $\overline{C}_{\ell mj}$ are Stokes coefficients with the overdot later used to indicate time differentiation. The index j is for the $\cos(m\lambda)$ or $\sin(m\lambda)$ parts of the SH expansion. While we are attentive to the full spectrum of ocean and atmospheric physics that can generate time-varying Stokes coefficients $\overline{C}_{\ell mj}$, we model only land-based cryospheric changes. These may drive either present-day surface density changes $\dot{\sigma}$ (θ, λ, t) at $r = R_E$ or mantle isostatic processes.

2.1.4. Advantages of Global Mascons

[10] The globality of the mascon ensemble minimizes leakage of signal from one region to another over continental scales, an error source that degrades the accuracy of past GRACE-based mass transport measurements [*Wahr et al.*, 2000; *Swenson and Wahr*, 2002; *Horwath and Dietrich*, 2009]. On a solid Earth of infinitesimal strain and linear constitutive law, a Love number formalism accounts for the observed external field [*Wahr et al.*, 1998; *Simon et al.*, 2010]. The technique is used in determining the mascon-specific time series without GIA corrections. The highest frequency variations in this series are caused by the atmospheric and oceanic mass changes. Variations that conserve mass allow the sum (1) to begin at $\ell = 1$.

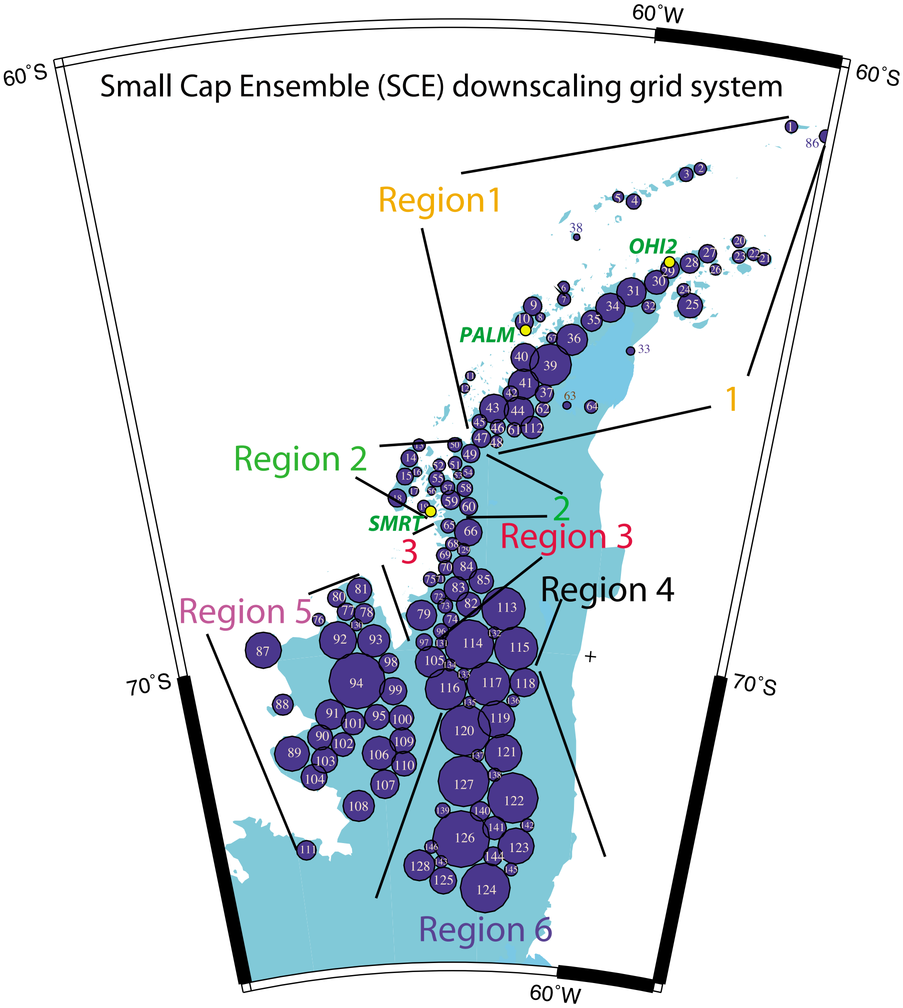

Figure 2. Regions for differing ice load models and numbered SCE grid system. Also shown (yellow dots) are the locations of the continuous GPS tracking stations employed in our uplift forward model solutions.

2.2. GPS Data: Antarctic Peninsula

[11] Robust vertical crustal motion trends have been demonstrated south of 65°S [e.g., *Tregoning et al.*, 2009]. The use of high-precision GPS satellite orbits over the course of past decade and a half have been encumbered by a number of difficulties. Foremost among recent breakthroughs are the treatment of (1) the inhomogeneity of the ground system hardware and software, (2) the inhomogeneities caused by the introduction of more advanced satellite systems ("blocks"), and (3) proper resolution of issues surrounding the evolution and self-consistency of the terrestrial reference frame. Theses difficulties are reconciled in a major reprocessing effort undertaken by the Technische Universität München (TUM), Technische Universität Dresden (TUD) and GeoForschungs-Zentrum (GFZ) Potsdam. The GPS data are treated by using the formal complete reprocessing method, starting with the raw observation data and simultaneously solving for orbits, clocks and station positions for each of 206 continuously operating globally distributed ground stations.

[12] The daily time series for trend in vertical position from three of these ground stations are in the Antarctic Peninsula. The International GNSS Service (IGS) station names are SMRT, PALM and OHI2, the later of which is a global fiducial site in the International Terrestrial Reference System (ITRS) defined by a GPS-only solution that has been described by *Steigenberger et al.* [2006] and *Rülke et al.* [2008]. The motions of the station coordinates are referenced to a center-of-mass system (CM), as described by *Rülke et al.* [2008] and *Rülke* [2009]. The CM system is also the frame from which GRACE data may self-consistently be described. This reference frame is determined by data from 1 January 1994 to 31 December 2005 and is referred to as "PDR05" (Potsdam-Dresden-Reprocessing TRF 2005) and is distinct from the standard and well-known ITRF2005 of *Altamimi et al.* [2007]. The core software analysis of GPS data has been described by *Dach et al.* [2007]. A synopsis of the reprocessing strategy is found in Table 1 of *Rülke et al.* [2008]. Some quantitative analyses of the improvement in orbital residuals using the reprocessing strategy is summarized by *Steigenberger et al.* [2009]. *Rülke et al.* [2008] note that vertical trends from 3.5 or more years of data may contain analysis-dependent errors as large as ±2 mm/yr. However, the vertical rates agree with Fennoscandian rebound models to within about 1 mm/yr. In this paper we will use the formal 1σ error statistics developed in the PDR05 analysis, but we

Table 1. Peninsula Vertical Velocities (mm/yr)[a]

Station	SMRT	PALM	OHI2
$\dot{u}^{rGPS}$ (this paper)	2.58 ± 0.29	4.98 ± 0.19	5.08 ± 0.26
Observing period	1993–2007	1993–2007	1993–2007
$\dot{u}^{rGPS}$ [*Bevis et al.*, 2009]	- -	4.8 ± 0.3	7.0 ± 0.7
Observing period	- -	1998–2008	2001–2008
Ice model III[b]	3.21	4.81	5.11

[a] Errors reported here are from formal RMS estimation.

[b] Fit assumes lithosphere thickness of 30 km, mantle viscosity $\eta = 7.5 \times 10^{19}$ Pa s.

extend the recomputation to include 26 December 1993 to 29 December 2007, or a 15 year long time series. Our model analysis has used both the more conservative rule of thumb (±2 mm/yr) for vertical error and the formal error statistics from the global analysis. The later contain relevant information about the overall quality of the small number of individual station time series. The results of the analysis depend little on which type of errors we assign to a simple χ^2 evaluation of the performance of forward models. In Table 1 the vertical uplift results are reported along side those recently published by *Bevis et al.* [2009], who used a quite different analysis strategy. Only the PDR05-based results are used in this paper. For the Patagonian Ice Field crustal motion observations a campaign-style set of quasi-continuous observations were employed and are described completely by *Dietrich et al.* [2010].

3. Past Glacial Load Forcing and GIA Response

3.1. Antarctic Peninsula and Patagonian Ice Field Ice Loads

[13] Glaciers of southern Patagonia and the Antarctic Peninsula are in distinctly different regional climate and cryospheric settings, in spite of both being affected by the Antarctic Circumpolar Current and Southern Annular Mode at the longitude of the Drake Passage. The ice fields of Patagonia consist of alpine glaciers. The annual mass balances of both tidewater and nontidewater glaciers may be analyzed by equilibrium theory for small mountain glaciers [e.g., *Naruse*, 1997; *Barcaza et al.*, 2009]. Classical mass balance analysis also applies to glaciers of the AP, but the strongest influence throughout the Antarctic Peninsula are ice shelf collapse events. The loss of the resistive ice shelf buttressing force upon collapse has caused land glaciers to accelerate their flow to the ocean since 1989 [e.g., *Skvarca et al.*, 1999; *Rignot et al.*, 2005; *Cook and Vaughan*, 2010].

3.1.1. Patagonia

[14] The model for reconstruction of the PIF we employ is described by *Dietrich et al.* [2010]. That model is rooted in backward extrapolation of present-day ice losses reported by *Rignot et al.* [2003] and updated by *Dietrich et al.* [2010]. In summary, the backward extrapolation relies using estimates to 1944, then using temperature recordings and the snout retreat-advance model of *Oerlemans* [2005]. A basic assumptions that length change is a simple proxy for differential mass rates, $\Delta\dot{M}(t)$, and that at Little Ice Age (LIA) maximum and a first-order nonlinear ordinary differential initial value problem is solved analytically with $\Delta\dot{M}(0) = 0$. We enforce the requirement that $\Delta\dot{M}(t_{\text{final}}) = \Delta\dot{M}_{\text{obs.}}$, where t_{final} and $\Delta\dot{M}_{\text{obs.}}$ are the time of the observations and mass loss rate value of *Rignot et al.* [2003], respectively. The key point is that the solutions are a guide to our back extrapolation of $\Delta\dot{M}$ and are directly linked to observations of the interannual changes in atmospheric temperature.

3.1.2. Antarctic Peninsula

[15] A somewhat analogous approach is employed for the Antarctic Peninsula, but without the *Oerlemans* [2005] theoretical basis. The model for reconstruction of the Antarctic Peninsula is initiated by assuming the land losses estimated by *Rignot et al.* [2008]. This estimate of $\Delta\dot{M}$ is backward extrapolated to the year 2002, the year of the dramatic collapse of the Larsen B Ice Shelf (LBIS in Figure 1, bottom insert). Naturally, we cannot use only this estimate for $\Delta\dot{M}$ since it is a quantity that we wish to extract from modeling GRACE and GPS data. The model for backward extrapolation cannot be overly complex, as this introduces far too many parameters to explain uplift of 3 GPS stations and a trend in GRACE gravity over 2003–2009.25. However, we are obliged to consider the mass changes that have occurred over at least the last 500–1000 years, as explained in detail elsewhere [e.g., *Ivins et al.*, 2000, 2002; *Larsen et al.*, 2005]. Most glaciers in the Antarctic Peninsula are known to have been receding in response to warming atmospheric temperature since about A.D. 1930. The first 20th century ice shelf breakup occurred in the late 1980s [*Rott et al.*, 2002]. The second backward extrapolation is to A.D. 1989, and similarly the 3rd, back to A.D. 1930.

[16] Extrapolation to a time of maximum LIA extent for the peninsula is more difficult. *Domack et al.* [1995] and *Hall* [2009] have cited clear evidence for a Little Ice Age in the AP, probably of longer duration than that of either Europe or Patagonia. *Hall et al.* [2010] have obtained radiocarbon dates indicating ice recession on Anvers Island (see “AI” in Figure 1) during A.D. 1030–1300, prior to the LIA. The LIA ice then advanced and latter began to dissipate sometime between A.D. 1850–1930. In contrast, *Domack et al.* [2005] has shown that on the eastern margin, Larsen Ice Shelf B (LISB in Figure 1, bottom insert) was stable throughout the middle to late Holocene (and by inference, also Larsen C and D). *Bentley et al.* [2009] notes that the solar insolation parameters controlled by planetary dynamics predict a cooling trend at 65°S. The insolation trend is corroborated by a number of paleoenvironmetal indicators, and a reasonable assumption is that the entire Antarctic Peninsula experienced neoglaciation after an early to mid-Holocene climate (warm) optimum when there was less land and ocean ice cover. For brevity, we do not give an extended discussion. Tables 2 and 3 give a synopsis of the general observations that guide the three contrasting ice models used for predicting the GPS vertical crustal motion data. We have chosen six regions (labeled “regions 1–6”) both for simplicity and for the fact that they represent different climatic zones of the peninsula. Justification for refinement into yet smaller regions requires improved spatial sampling by GPS.

3.2. Theory: The Small Cap Ensemble

[17] The glacier-specific smaller spherical caps form a spatial ensemble, shown for the AP, for example, in Figure 2. For Patagonia these correspond to the areas covered by specific glaciers for which mass balance estimates are available [*Rignot et al.*, 2003; *Dietrich et al.*, 2010]. Each cap is of constant radius α_i in time, but of time-varying height,

Table 2. Primary Pre-LIA to Post-LIA Coastal Ice Cover Changes North of 68°S

Ice Shelf	Mid-Holocene	LIA	Post-LIA	1989–2002
		Region 1		
Prince Gustav	5–2 ka collapse[a]	maximum[b]	retreat[c]	collapse 1995[c]
Larsen A	collapse[d]	advance post-1.4 ka[e]	retreat	ice free
Larsen B and northern C	stable[f]	stable[f]	stable[f]	collapse 2002[c]
Offshore Anvers Island[b]	advance post-3.4 ka[g]	maximum[h]	ice free	ice free
		Region 2		
Müller	neoglaciation[i]	advance[j]	minor retreat[c]	stable[c]
Jones	–	stable	stable until 1978[c]	ice free[c]

[a] *Pudsey and Evans* [2001] and *Pudsey et al.* [2006].
[b] *Hall* [2009].
[c] *Cook and Vaughan* [2010].
[d] *Hodgson et al.* [2006].
[e] *Bentley et al.* [2009].
[f] *Domack et al.* [2005].
[g] *Domack et al.* [2001].
[h] *Hall et al.* [2010].
[i] *Allen et al.* [2010].
[j] *Domack et al.* [1995].

$\dot{D}_i^{(p)}$ during P discrete time epochs; $t_{p-1} \le t \le t_p$, where the last period, $t_{P-1} \le t \le t_P$ corresponds to the GRACE observing period, and at some time $t \ge t_{P-1}$ the model also incorporates the GPS trends. The ensemble caps for GL and NPI+SPI are only loosely analogous to the continental-scale spatial averaging kernels used for Antarctic trend studies [*Velicogna and Wahr*, 2006; *Horwath and Dietrich*, 2009]. Each model produces a different sum over all mass cap increments, $\dot{M}_i^{(P)} \equiv \rho_{ice}\pi\dot{D}_i^{(P)}\alpha_i^2$, covering our GRACE observations. The radii, α_i, of AP caps vary from 5.5 to 50 km, and average about 14 km. In the NPI+SPI these are smaller by about a factor of 2. The small dimensions of these caps necessitate the use of half-space viscoelastic computations for GIA response [*Ivins and James*, 1999]. The magnitude of the effects of sphericity and upper-lower mantle stratification were estimated using spherical Earth model computations [*Ivins et al.*, 1993]. The latter effects are negligible when we use the resultant GIA corrections to determine present-day mass secular variability that is limited to the spatial area of individual mascons and their nearest neighbors.

[18] Among the six regions shown in Figure 2, consecutive back extrapolations from P to $P - 1$, and so on, assume increments of constant $\dot{M}^{(p)}$ for the sum of cap contributions from each individual region. This provides the basis for constructing a height history of piecewise linear $D_i^{(p)}$. Thus, for each step p, $\dot{D}_i^{(p)}$ are assumed homogeneous within each region.

3.3. Theory: Present-Day Glacial Load Forcing

[19] Conventional practice adopted by the various GRACE analysis centers has been to provide gridded or SH solutions as WHE. This inherently assumes that the elastic yielding effects of surface loading are removed. If we are to correct trends in water equivalent height for GIA and then correct and restore the results to the original intent of the release, we must correctly define surface mass effects with and without (rigid) elastic correction. Ultimately, it is important to show some of the discrepancies in using a GIA correction to restore water mass equivalency (here conveyed as "WHE") on a rigid Earth, which is the goal of most cryospheric scientists in using GRACE data.

3.3.1. Surface Mass

[20] It is straightforward to convert volumetric ice imbalances that are a function of surface coordinates and time (θ, λ, t) into gravity and crustal motion for elastic Earth models. First, we note that a set of surface density rate

Table 3. Primary Pre-LIA to Post-LIA Coastal Ice Cover Changes South of 68°S

Ice Shelf	Mid-Holocene	LIA	Post-LIA	1989–2002
		Region 3		
Wordie	advance post-2.8 ka[a]	maximum[a]	retreat	retreat
Central Larsen C	stable	stable	stable[b c]	stable
		Regions 4 and 5		
George VI	advance post-3.8 ka[d]	maximum	retreat	retreat
Wilkins	advance post-4.4 ka[d]	stable	stable to 1991	rapid retreat[e]
Northern Larsen D	stable	stable	stable[b]	stable
Bach and Stange	–	–	retreat[c]	retreat[c]
		Region 6		
George VI (south)	advance post-3.8 ka[d]	maximum	retreat	retreat
Central Larsen D	stable	stable	stable[c]	stable

[a] *Domack et al.* [1995].
[b] *Domack et al.* [2005].
[c] *Cook and Vaughan* [2010].
[d] *Bentley et al.* [2005].
[e] *Braun et al.* [2009].

coefficients, $\dot{\overline{\sigma}}_{\ell mj}$ [see *Ivins et al.*, 1993, equation (22)], may be calculated in an expansion similar to (1) and related to Stokes rate coefficients for a rigid Earth as

$$\dot{\overline{\sigma}}_{\ell mj} = \frac{M}{2\pi R_E^2}\left(\ell + \frac{1}{2}\right)\dot{\overline{C}}^{load}_{\ell mj}, \tag{2}$$

where $\dot{\overline{C}}^{load}_{\ell mj}$ are the time-trended Stokes gravity rate coefficients on a rigid Earth (wherein elastic yielding has been corrected for).

[21] With a direct and uniform loading of the ocean at sea level rise rate, $\dot{\xi}$, these coefficients can be computed from a series of glacier-specific spherical caps with rates of ice height changes $\dot{D}_i^{(p)}$ with the density coefficients $\dot{\overline{\sigma}}_{\ell mj}$. Independent mass balance mapping [e.g., *Rignot et al.*, 2008; *Riva et al.*, 2009] can be one basis for constructing an ab inito set of coefficients $\dot{\overline{\sigma}}_{\ell mj}$. During the observation period, $t_P - t_{P-1}$, of GRACE and GPS trend solutions, the forward model of mass transfer to the oceans conserves mass by introducing the ocean function. The result is

$$\dot{\overline{\sigma}}_{\ell mj} = \rho_{\text{ice}} \sum_{i=1}^{\mathcal{I}_{\text{disk}}} \tilde{w}_{\ell mj,i}\dot{D}_i^{(P)} - \frac{\rho_{\text{w}}}{2\ell+1}\dot{\xi}\overline{a}_{\ell mj}, \tag{3}$$

where ρ_{w} and ρ_{ice} are densities of ocean water and continental ice, and $\overline{a}_{\ell mj}$ are the standard normed ocean coefficients, entering as mass conservation terms in the land-ocean transport process [e.g., *Lambeck and Cazenave*, 1976]. The total number of caps is $\mathcal{I}_{\text{disk}}$ and $\tilde{w}_{\ell mj,i}$ are cap coefficients [*James and Ivins*, 1998].

3.3.2. Geodetic Predictions With Elastic Yielding

[22] The rate of change of the geoid height and surface vertical displacements are

$$\dot{\mathsf{N}}(\theta,\lambda,t) = R_E \sum_{\ell=1}^{L}\sum_{m=0}^{\ell}\sum_{j=1}^{2} \dot{\overline{C}}^{load}_{\ell mj}(t)(1 + k_\ell{}')\overline{Y}_{\ell mj}(\theta,\lambda) \tag{4}$$

and

$$\dot{\mathsf{u}}^{\mathsf{r}}(\theta,\lambda,t) = R_E \sum_{\ell=1}^{L}\sum_{m=0}^{\ell}\sum_{j=1}^{2} \dot{\overline{C}}^{load}_{\ell mj}(t)h_\ell{}'\overline{Y}_{\ell mj}(\theta,\lambda), \tag{5}$$

respectively. Elastic deformation is accounted for by the surface potential and radial displacement surface load Love numbers, k'_ℓ and h'_ℓ, respectively. Note that with sufficient time span for GPS observations, a surface load-driven rate of radial displacement may be related to the Stokes load coefficients in equation (5) [*James and Ivins*, 1998] or to those generated by GIA [*Tregoning et al.*, 2009]. When an elastic response for the solid Earth is assumed, equations (5) and (6) tie together GRACE and GPS analyses. For example, this link was exploited in a recent study of Greenland by *Khan et al.* [2010]. However, in Patagonia, a region of recent subduction of a warm and volatile-rich ocean ridge, *Dietrich et al.* [2010] demonstrated that the elastic response approach cannot explain the regional GPS uplift data. The similarities of recent tectonics and upper mantle beneath the NPI+SPI and AP ice masses strongly suggests that the assumption of elastic response is a poor assumption for both regions. GIA involves a viscoelastic deformation theory [*James and Ivins*, 1998; *Ivins and James*, 1999] and no simple relation like (5) applies. We give the elastic surface load Love numbers in the theory above simply for clarity.

3.4. Time Series Analysis in the Spherical Spectral Domain

[23] The GLM is used to generate a synthetic set of range rate and range accelerations and a large matrix containing all mascon-specific information is then used to invert for masses associated with each mascon cap. Collectively, these inverted-for masses form the time series, and they are the essential backbone for the creation of monthly fields $\mathcal{T}$ (assumed mapped to $r = R_E$ as in equation (1)). The generation of the separated trend coefficients, $\dot{\overline{C}}^S_{\ell mj}$, then logically follows. The GLM time series of Stokes coefficients (superscripted "Mc") is decomposed as

$$\overline{C}^{Mc}_{\ell mj}(t) = \Delta\overline{C}^{o}_{\ell mj} + \dot{\overline{C}}^{S}_{\ell mj}\cdot t + \sum_{\kappa=1}^{\mathrm{K}} \overline{C}^{\kappa}_{\ell mj}\cos\left[2\pi f_\kappa t + \phi^\kappa_{\ell mj}\right], \tag{6}$$

where the first term is a simple offset, $\Delta\overline{C}^o_{\ell mj}$, the coefficient superscript "*S*" is the "secular" rate, and the sum on κ is formed from the decomposition of semiannual, annual, S_2, and K_2 tidal alias terms [*Ray and Luthcke*, 2006] plus any additional known frequencies, f_κ. For each SH (ℓmj) these amplitudes, $\overline{C}^\kappa_{\ell mj}$, and phases, $\phi^\kappa_{\ell mj}$, are solved for in a least squares sense using the algorithms of *Hanson and Lawson* [1969]. A principal goal of the time series analysis is to obtain $\dot{\overline{C}}^S_{\ell mj}$ with as little corruption from interannual oscillations as possible. A distinct 2.6 year hydrological periodicity has been identified in a wavelet analysis of proglacial lake level data in Patagonia [*Pasquini et al.*, 2008] and we include this as a potential corrupting frequency. Solving and removing SH components near this period produced small (~1–2%) improvements to the secular trends, $\dot{\overline{C}}^S_{\ell mj}$. It is, however, important to examine the full raw time series, $\dot{\overline{C}}^{Mc}_{\ell mj}(t)$, without decomposition. In Figure 3a we give the 6.25 year long unfiltered time series retrieved in the target regions where the solid line represents the sum of all solved-for amplitudes and phases represented here in the spatial domain at positions for the AP, precisely in the BP, upstream of the glaciers that feed into the partially collapsed ice shelves on the eastern coastal boundary (Figure 1) and for the SPI, in the central-north SPI (Figure 1). This result is uncorrected for GIA. In Figure 3b the regionally filtered data, uncorrected for GIA, are shown with the least squares trend solutions. By "unfiltered" we mean that none of the periodic terms solved for by applying least squares to the time series of SH coefficients have been removed. Global maps for both trend and the amplitude of the longest solved-for periodic component are shown in Figure 4.

[24] In the following, our focus is on the sustained change in 6.25 years, and we set $\dot{\overline{C}}^{load}_{\ell mj} = \dot{\overline{C}}^S_{\ell mj}$, the surface-only component of the potential field and we note that $\dot{\overline{C}}^{load}_{\ell mj}(t) = \dot{\overline{C}}_{\ell mj}(t)(k'_\ell + 1)^{-1}$ only if deep-seated viscoelastic flow is negligible.

4. Model GIA and Present-Day Mass Loss $\Delta\dot{M}$

[25] GIA is caused by slow motion in a highly viscous mantle, gravitationally responding to large-scale ice mass variability of the past. The flow in a density-layered Earth

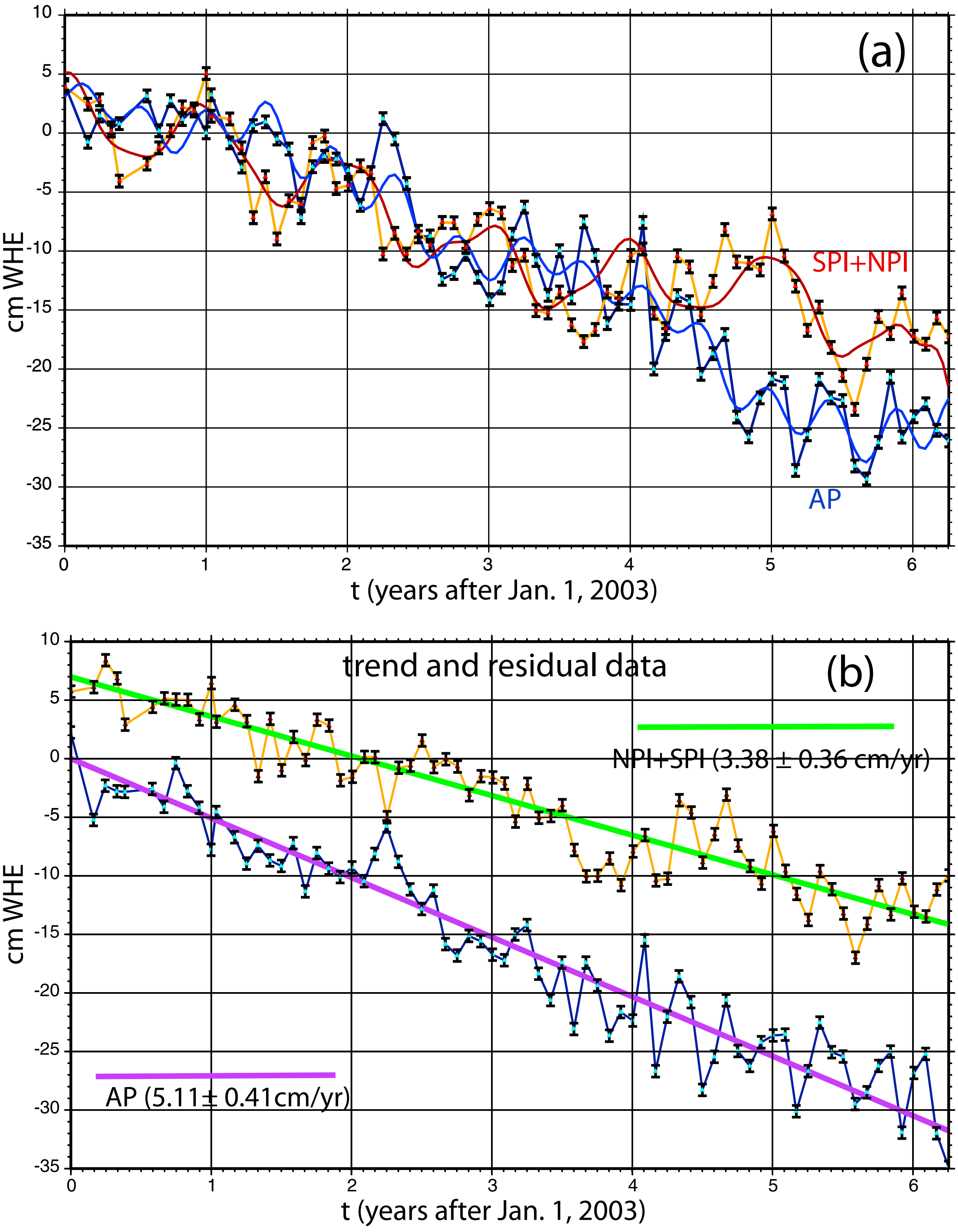

Figure 3. Time series of monthly mascon solutions for SPI+NPI and AP. These solutions are recovered from the sums on SH representations truncated to degree and order 120 with a Gauss-smoothing radius of $\lambda_G = 225$ km. (a) The periodic plus linear trend functions retrieved by a least squares fit to these regionalized data with the same functions as in equation (6) (shown in red and blue for the two regions, respectively). (b) The linear trend with periodic terms removed from the data. These pre-GIA corrected mascon solutions used interannual climate periodicities of 2.6 years for AP and 3.1 years for NPI+SPI, as these produced the smallest residuals, respectively. The climate periodicity for the NPI+SPI differ from the 2.6 years used for the global solutions in the SH domain.

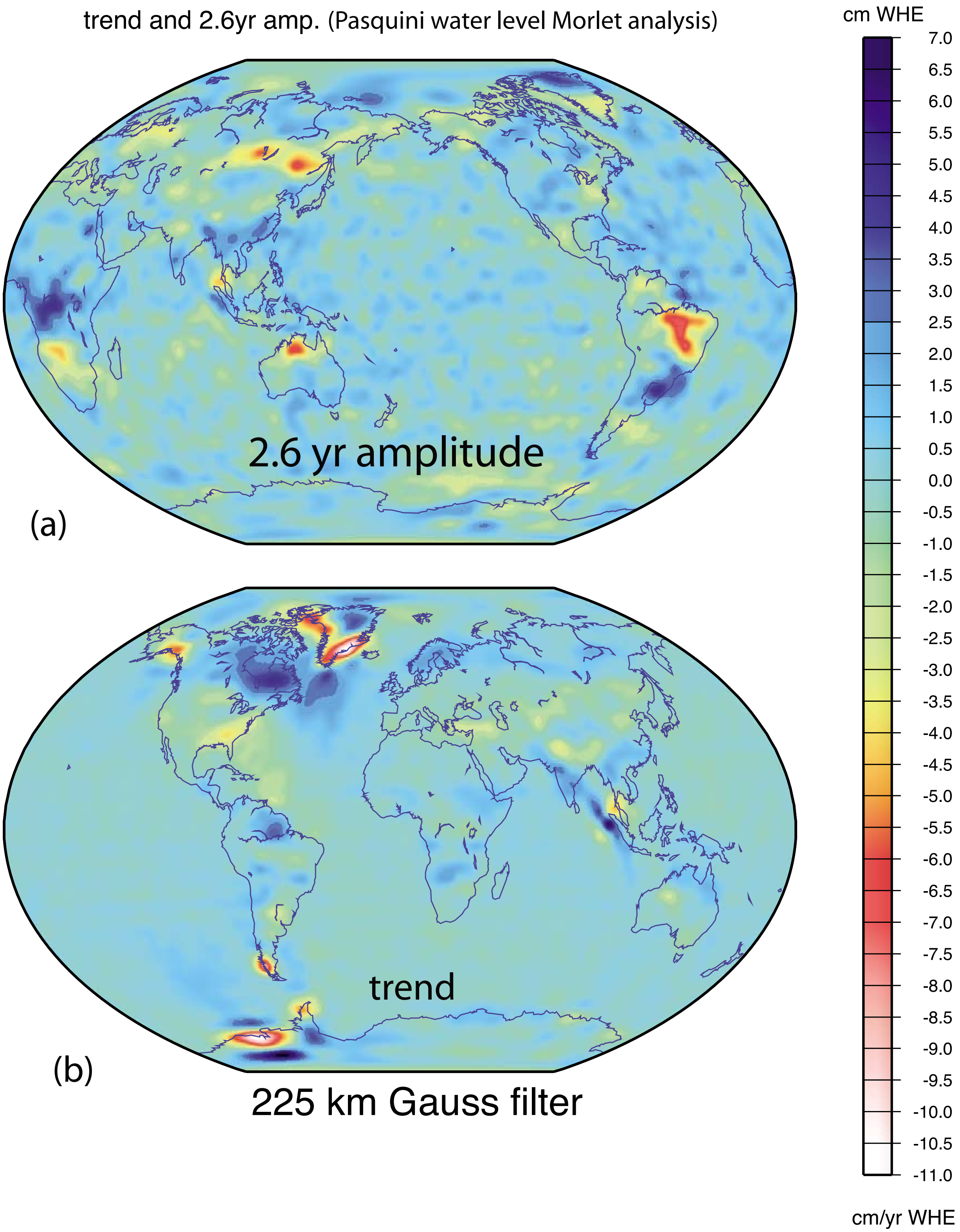

Figure 4. (a) Amplitude for a preselected low frequency corresponding to a lake level study [*Pasquini et al.*, 2008] and (b) the trend as resolved from equation (6). Note that the amplitude of the 2.6 year term in Figure 4a is referred to an SH set of components. The map is produced using $\sum_{\ell,m,j}^{L,\ell,2} \overline{C}^{\kappa}_{\ell mj} \overline{Y}_{\ell mj}(\theta, \lambda)$ with κ corresponding to a 2.6 year component.

strives to reestablish gravitational equilibrium, even when surface load variability may have waned many hundreds to thousands of years ago. The improved accuracy and stability of GPS solutions are now the key tool for disentangling Antarctic GIA and from satellite gravity determined ice mass trends [*Tregoning et al.*, 2009]. Here we explicitly employ new isostatic uplift constraints provided by GPS in the SPI [*Dietrich et al.*, 2010] and GL [*Rülke et al.*, 2008].

[26] The sequence of P modeled change in mass M drive the predicted GIA gravity change and deformation. Model GIA uplift prediction depends upon the entire sequence of assumed mass loss/gain rates (and their duration) and mantle rheology (as parameterized by lithosphere thickness, h, and mantle viscosity η). Uplift can be recast as WHE, then smoothed by truncation at maximum order, L = 120, of the spherical harmonic (SH) representation of the field at a level comparable to the GLM resolution. The relevant loading-unloading sequences in Patagonia and the Antarctic Peninsula require that the load be resolved to high degree and order spherical harmonic ($L = M \approx 1900$). Consequently, we compute the GIA models in a half-space geometry with cylindrical coordinates. The predicted uplift at the time $t = t_{\mathrm{obs}}$ can be expanded in spherical harmonics using the expansion

$$\dot{\mathsf{u}}^{\mathsf{r}}(\theta, \lambda, t_{\mathrm{obs}}) = \sum_{\ell=1}^{L}\sum_{m=0}^{\ell}\sum_{j=1}^{2} \dot{\mathsf{u}}^{\mathsf{r}}_{\ell mj}\overline{Y}_{\ell mj}(\theta, \lambda), \tag{7}$$

using numerical integration. The secular rate of change in geoid caused by the motion of the solid Earth is

$$\dot{\mathsf{N}}^{GIA}(\theta, \lambda, t_{\mathrm{obs}}) = R_E \sum_{\ell=1}^{L}\sum_{m=0}^{\ell}\sum_{j=1}^{2} \dot{\overline{C}}^{GIA}_{\ell mj}\overline{Y}_{\ell mj}(\theta, \lambda), \tag{8}$$

and a reasonable approximation [*Wahr et al.*, 2000; *Tregoning et al.*, 2009] is

$$R_E \dot{\overline{C}}^{GIA}_{\ell mj} \cong \left(\ell + \frac{1}{2}\right)^{-1} \dot{\mathsf{u}}^{\mathsf{r}}_{\ell mj}. \tag{9}$$

Truncation for the purposes of analysis with the GRACE mascon fields uses $L = M = 120$. The GIA correction then takes the form of a subtraction of $\dot{\overline{C}}^{GIA}_{\ell mj}$ from each GRACE mascon derived Stokes secular rate coefficient. Within each computed field $\dot{N}^{GIA}$ (θ, λ, t_{obs}) is a modeled assumption of distributed landmass loss, as implied by equation (3). The GIA correction to GRACE for obtaining surface mass trend is formally summarized as

$$\dot{\overline{C}}^{load}_{\ell mj} \equiv \dot{\overline{C}}^{S}_{\ell mj} - \dot{\overline{C}}^{GIA}_{\ell mj}. \tag{10}$$

4.1. Antarctic Peninsula: Initial Iterations to Present-Day Mass Loss $\Delta\dot{M}$

[27] Successful solutions $\Delta\dot{M}$ during the GRACE observing period must be compliant with both GPS and GRACE mascon trends. Compliant uplift models then also yield a GIA correction for deriving the total regional mass loss rate, $\Delta\dot{M}$, over the period of combined observation. Each $\Delta\dot{M}$ solution may be improved upon, either by updates to load history or to mantle-lithosphere rheology. The GPS data and some basic constraints on past ice mass changes are critical to a stable iteration. It is also important to later show the GIA-corrected solutions represented on an entirely rigid Earth, employing the identical discrete cap structure as in Figure 2, using identical filtering. We performed approximately 200 iterations in a random walk manner, each updated load and Earth parameter model was selected based upon the success of previous estimates. The initial estimate of $\Delta\dot{M}$ is taken from an extrapolation by *Rignot et al.* [2008] for the entire Peninsula at $\Delta\dot{M} = -60 \pm 46$ Gt/yr and for GL separately -47 ± 9 Gt/yr. After 30–40 iterations it became clear that the loss rate $\Delta\dot{M}$ over the GRACE observation period needed to be reduced to below $|-50|$ Gt/yr, but above $|-31|$ Gt/yr. Given the range and uncertainty in Earth parameters and LIA through 20th Century, we selected a value of -41.5 ± 9 for the ice load model and then reexamined the quality of the fit to the GPS data by sweeping through ice load models and Earth parameter variability. Comparison of formal χ^2 fits to the GPS data was used for this refinement. It was also estimated that GL had a range of $\Delta\dot{M}$ values between about -26 to -38 Gt/yr, somewhat lower than the estimate of *Rignot et al.* [2008]. In the parameter study the regionalization of the load model indicated in Figure 2 was employed.

4.2. Patagonian Ice Fields: Present-Day Mass Loss $\Delta\dot{M}$

[28] The locations of the SPI+NPI stations are designed specifically for the purpose of observing GIA [*Dietrich et al.*, 2010]. The data lack the spatial fidelity for fully constraining GIA, and hence we are obliged to forward model, and backward adjust, simple models that allow some variability in load history, mantle viscosity and elastic lithosphere thickness [*Ivins and James*, 1999; *Dietrich et al.*, 2010]. Using forward model iteration procedures, a mass loss distribution from balance studies for the periods 1995–2000 and 1975–2000 for SPI and NPI, respectively [*Rignot et al.*, 2003; *Dietrich et al.*, 2010] was assumed. Here the dimensions of individual glaciers are approximated as 119 discrete caps. Details of the load-modeled uplift data are given elsewhere for the SPI+NPI [*Dietrich et al.*, 2010]. An essential part of our story is to give a rough a priori consideration of the last 500 years of regional ice history. The models assume ice growth prior to the LIA, followed by an equilibrium state, then terminating at about A.D. 1870 in SPI+NPI and GL [*Masiokas et al.*, 2009; *Ivins and James*, 1999; *Dietrich et al.*, 2010]. Readjustment of the $\Delta\dot{M}$ estimated by *Rignot et al.* [2003] and later by *Dietrich et al.* [2010] was negligible, as the model had already been adjusted as an optimum fit to the GPS data. The GIA correction values for Patagonia are discussed in section 6.3.

5. Earth Parameters, Load History, and GIA-Corrected Trends

5.1. Antarctic Peninsula: Load Models

[29] Although there are undoubtedly additional models that could be investigated, three models are used here to highlight some important sensitivities of the GPS data to Earth parameters. The first has a Patagonian-style entry into, and exit from, the LIA. Ice begins to retreat starting in A.D. 1850, after some several hundred years of advancement. Figure 5 shows the mass changes associated with the first history (model I).

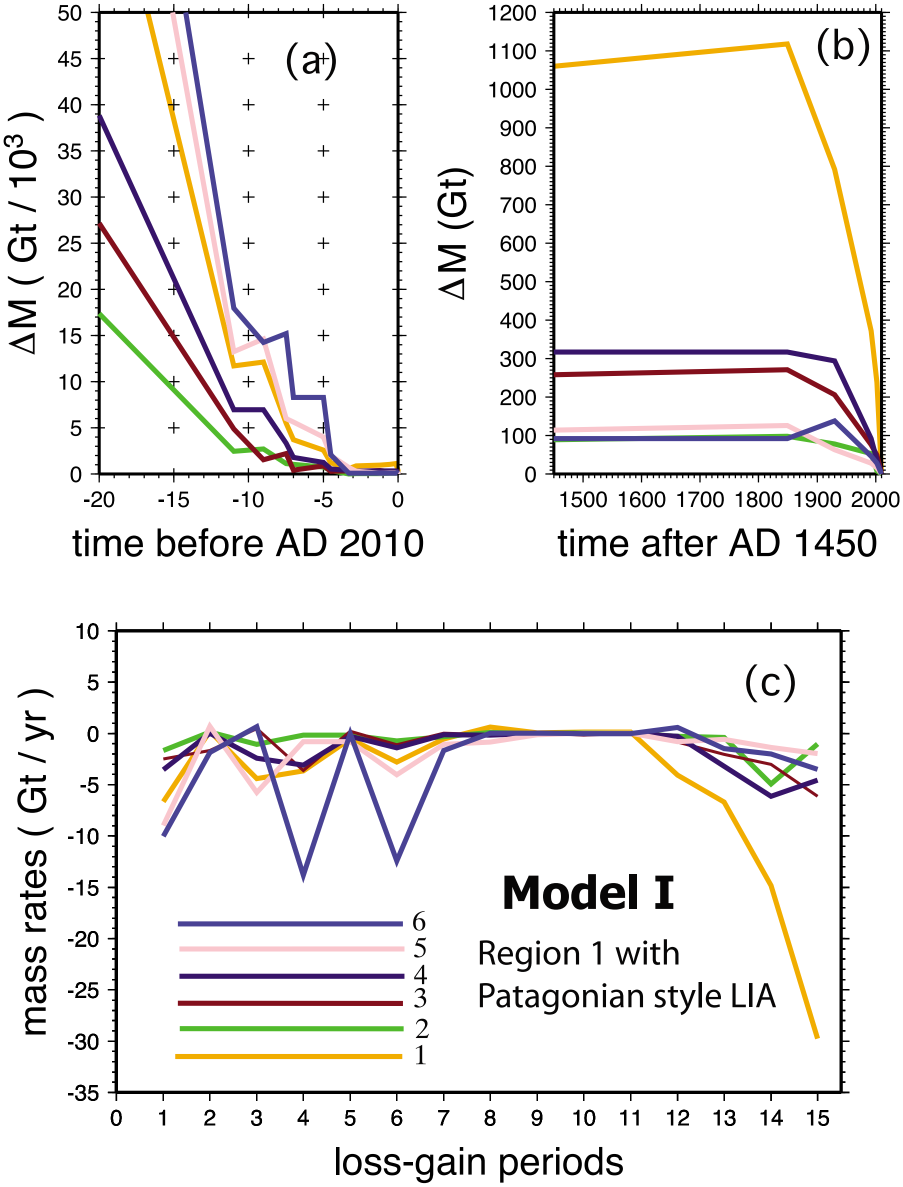

Figure 5. Model I load history for the six regions. The color coding corresponds to that of Figure 2. LIA in model I terminates at A.D. 1850, except in region 4. All regions have loss after A.D. 1930. Table 2 gives observational rationale for models I–III.

This model accommodates an increase in rate at A.D. 1930 and all regions initiate mass losses at 160 years B.P. (except in region 4). Model I has an extended LIA growth period as advocated in some paleoclimate scenarios [e.g., *Bentley et al.*, 2009; *Hall et al.*, 2010]. In model I the dominant region of change is in GL (region 1). Model II (see Figure 6) assumes a more evenly distributed set of mass changes throughout the Antarctic Peninsula, and an LIA duration that is more sharply defined in time. Region 6, it should be noted, includes the location of the recent δ^{18}O data extracted from the Gomez ice core which indicates warming since A.D. 1900 [*Thomas et al.*, 2009]. Finally, model III (see Figure 7) introduces a cold and relatively stable GL (region 1), along with the remainder of the Antarctic Peninsula, until the year A.D. 1930. The later model is supported by δ^{18}O ice core data collected south of GL in the Dyer Plateau (DP) (see Figure 1) [*Thompson et al.*, 1994]. For each model the total Peninsula mass loss during the observing period is −41.5 ± 9 Gt/yr.

5.2. Antarctic Peninsula: Results for Earth Parameter Estimation.

[30] Although a more extensive set of GPS stations exist in the GL, and to the south, the data suffer from a number of other error sources and their one σ trend errors are ±2.5 mm/yr. Initially we assumed errors of this magnitude for the first phase of the parameter search (~200 iterations). A refinement of the estimated parameters, assuming load models I–III, uses the formal errors reported in Table 1.

[31] The two solid Earth parameters adjusted in the half-space model are the lithospheric thickness h and the half-space viscosity, η. Investigation of lower mantle viscosity in a multilayer layer spherical model, indicated that the main

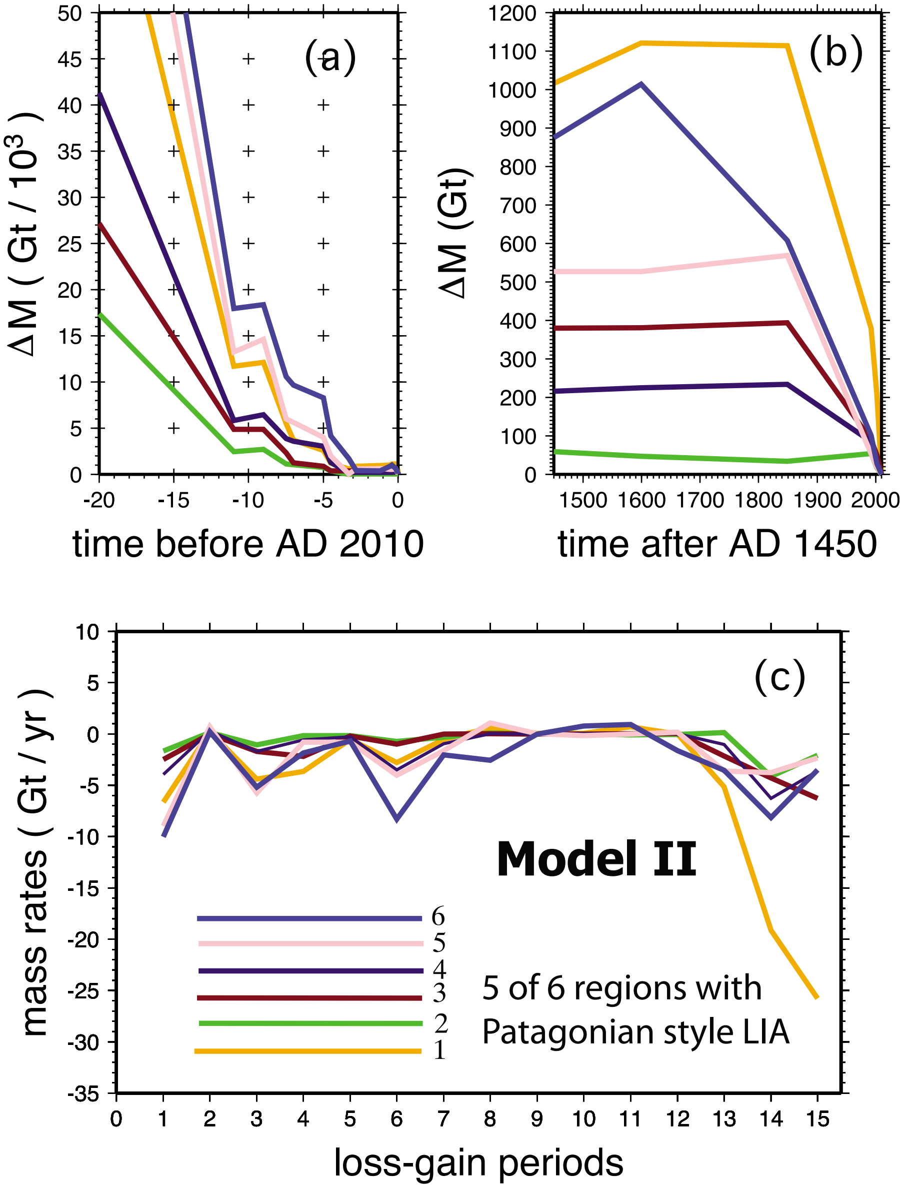

Figure 6. Model II load history for the six regions. LIA collapse initiates at A.D. 1850 and is constant in mass rate loss until A.D. 1993.

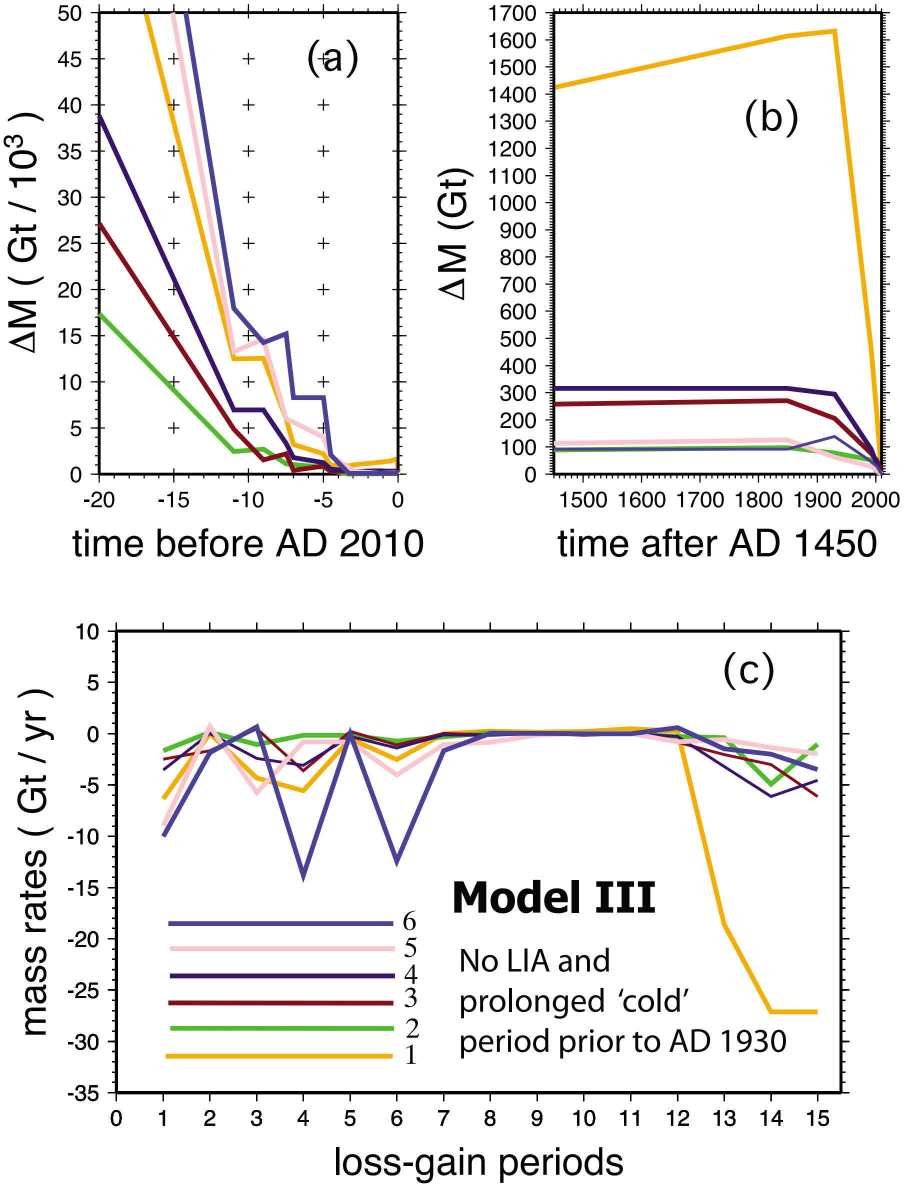

Figure 7. Model III load history for the six regions. A long LIA is confined to region 1, and there is no collapse for any region prior to A.D. 1930.

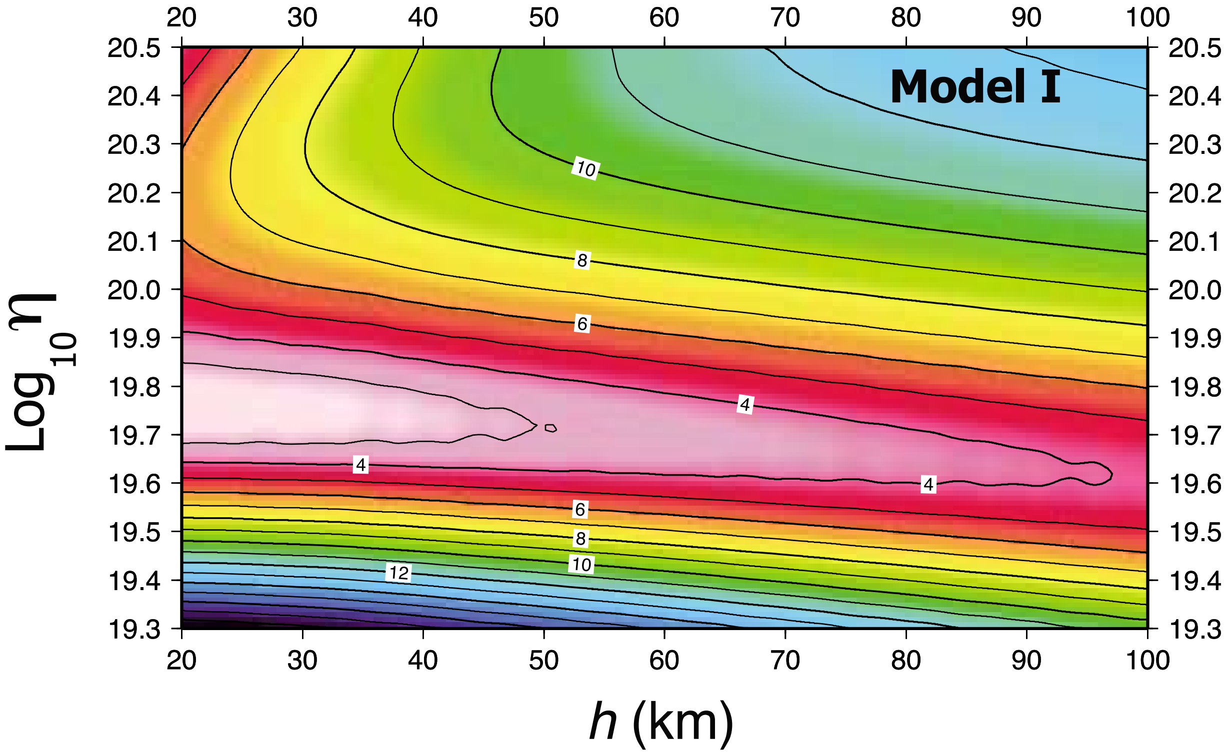

Figure 8. The χ^2 contours for model I load history and viscosity-lithospheric thickness parameter variations.

effect predicts a somewhat uniform offset in vertical velocity, generally with 1 mm/yr higher a predicted response rate. Tests with a layered spherical code [*Ivins et al.*, 1993] provided this estimate. Inclusion of layered structure in the top 450 km of the upper mantle could change our radially averaged parameter determinations for h and η. This will be discussed further in the conclusions.

[32] Model I and II χ^2 plots are shown in Figures 8 and 9. While model I performs slightly better than model II at minimizing χ^2, the results are not significantly different: $3 \times 10^{19} \leq \eta \leq 8 \times 10^{19}$ Pa s and $20 \leq h \leq 45$ km for the former and $4 \times 10^{19} \leq \eta \leq 7 \times 10^{19}$ Pa s and $20 \leq h \leq 50$ km for the later.

[33] With the exception of regions 2 and 5 (which have relatively small ΔM contributions), model III has unloading of all areas including GL (region 1) at 80 years after those of models I and II. This difference does make a more substantial difference in the Earth parameter estimation results. For model III the χ^2 is minimized for $5 \times 10^{19} \leq \eta \leq 1 \times 10^{20}$ Pa s and $20 \leq h \leq 90$ km (see Figure 10). Generally, the derived constraints on h are quite broad and it should be noted that the maximum depth of seismicity southeast of the South Shetland Islands (Figure 1) is about 30 km [*Robertson Maurice et al.*, 2003]. The best χ^2 fits in Figures 8–10 are consistent with the value $h \approx 30$ km. Model III minimum χ^2 results are reduced by a factor of 2 below those of model I and II fits, suggesting that the assumption of an extended cold period to A.D. 1930 is more consistent with the GPS vertical rates than are those having earlier deglaciation.

5.3. Water Height Rates

[34] One goal of the GRACE mission is to provide the land hydrology community with cross-discipline model output parameters. Toward this goal, satellite solutions report results in "water height equivalent" (WHE) change, $\dot{\mathsf{h}}$. For example, this is a quantity that readily allows comparison to ice height changes (accounting for density differences between water and snow/ice) using WHE rate maps. The maps are constructed from

$$\dot{\mathsf{h}}(\theta, \lambda, t) = \sum_{\ell=1}^{L}\sum_{m=0}^{\ell}\sum_{j=1}^{2}\dot{\mathsf{h}}_{\ell mj}^{H_2O}(t)\overline{Y}_{\ell mj}(\theta, \lambda), \tag{11}$$

where the WHE rate coefficients are

$$\dot{\mathsf{h}}_{\ell mj}^{H_2O} = \frac{(2\ell+1)}{3}\frac{\overline{\rho}_e}{\rho_w}R_E\mathsf{W}_\ell(\lambda_G)\dot{\overline{C}}_{\ell mj}^{load}, \tag{12}$$

where $\overline{\rho}_e$ is the mean density of the Earth. Here we introduce the isotropic Gaussian averaging, W_ℓ (λ_G), effectively down-weighting higher spherical harmonics. It is related to resolution wavelength kernel, λ_G [*Wahr et al.*, 1998]. For GRACE analysis, generally, 400 km $\leq \lambda_G \leq$ 900 km [*Schrama et al.*, 2007]. For GLM, however, the half width of our resolving wavelength is $\Delta\lambda \simeq 210$ km, and, therefore, the iteration scheme assumes 200 km $\leq \lambda_G \leq$ 250 km. Equations (2)–(12) show that linear relations exist among all coefficient representations. These relations also link the mascon-retrieved $\overline{C}_{\ell mj}^{S}$ coefficients determined by the microwave intersatellite ranging data with the GPS uplift data and GIA correction.

5.4. Map View Predictions

[35] Figure 11 shows map views of various stages of the iteration process for the Antarctic Peninsula (Figures 11a

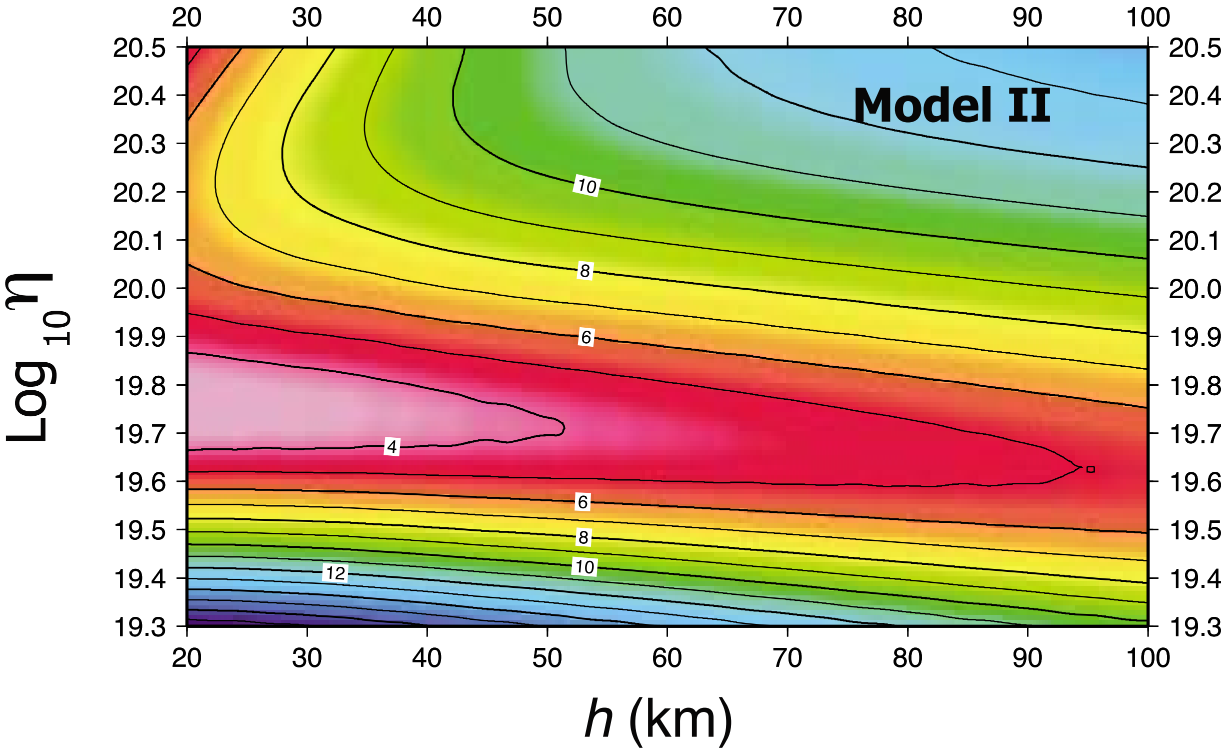

Figure 9. The χ^2 contours for model II load history and viscosity-lithospheric thickness parameter variations.

and 11b) and Patagonia (Figure 11c). The uplift rate predicted in Figure 11a is after about 60 forward model iterations and used the errors on GPS vertical rates as 2.4 mm/yr, a level of accuracy now generally achievable in the polar cryospheric environment [e.g., *Amalvict et al.*, 2009; *Tregoning et al.*, 2009; *Khan et al.*, 2010]. An ice chronology similar to model II (Figure 6) is assumed, the model differing in that the total loss during 2002–2009 for the whole of the Antarctic Peninsula is −46 Gt/yr and the SCEs on Adelaide Island have a slight increase in mass until 1993. GPS stations are located

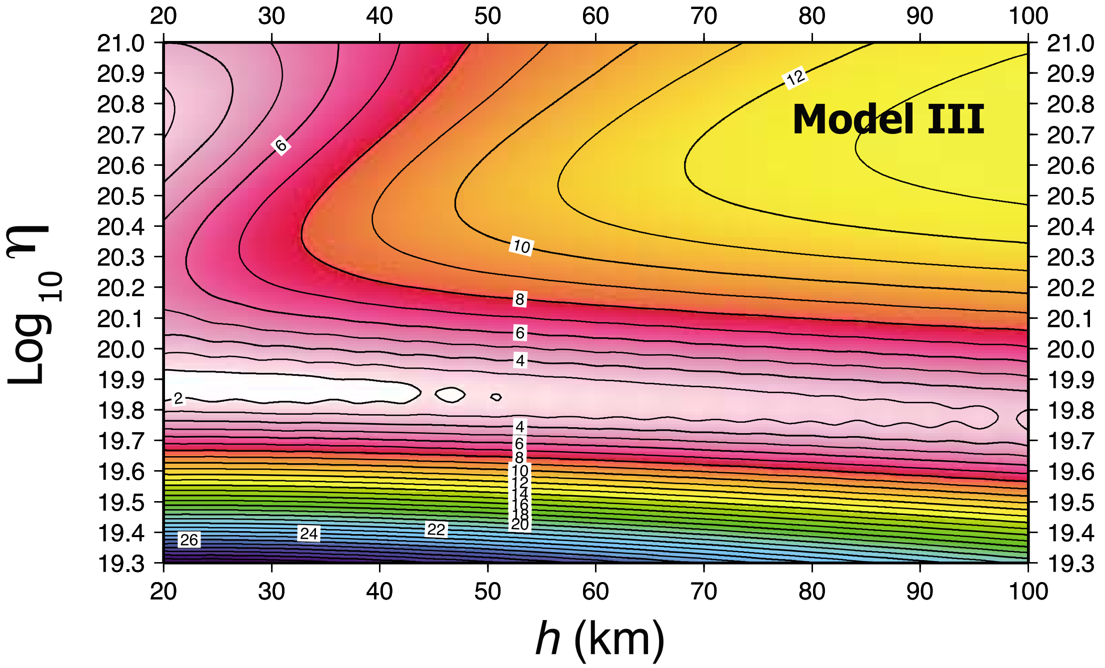

Figure 10. The χ^2 contours for model III load history and viscosity-lithospheric thickness parameter variations.

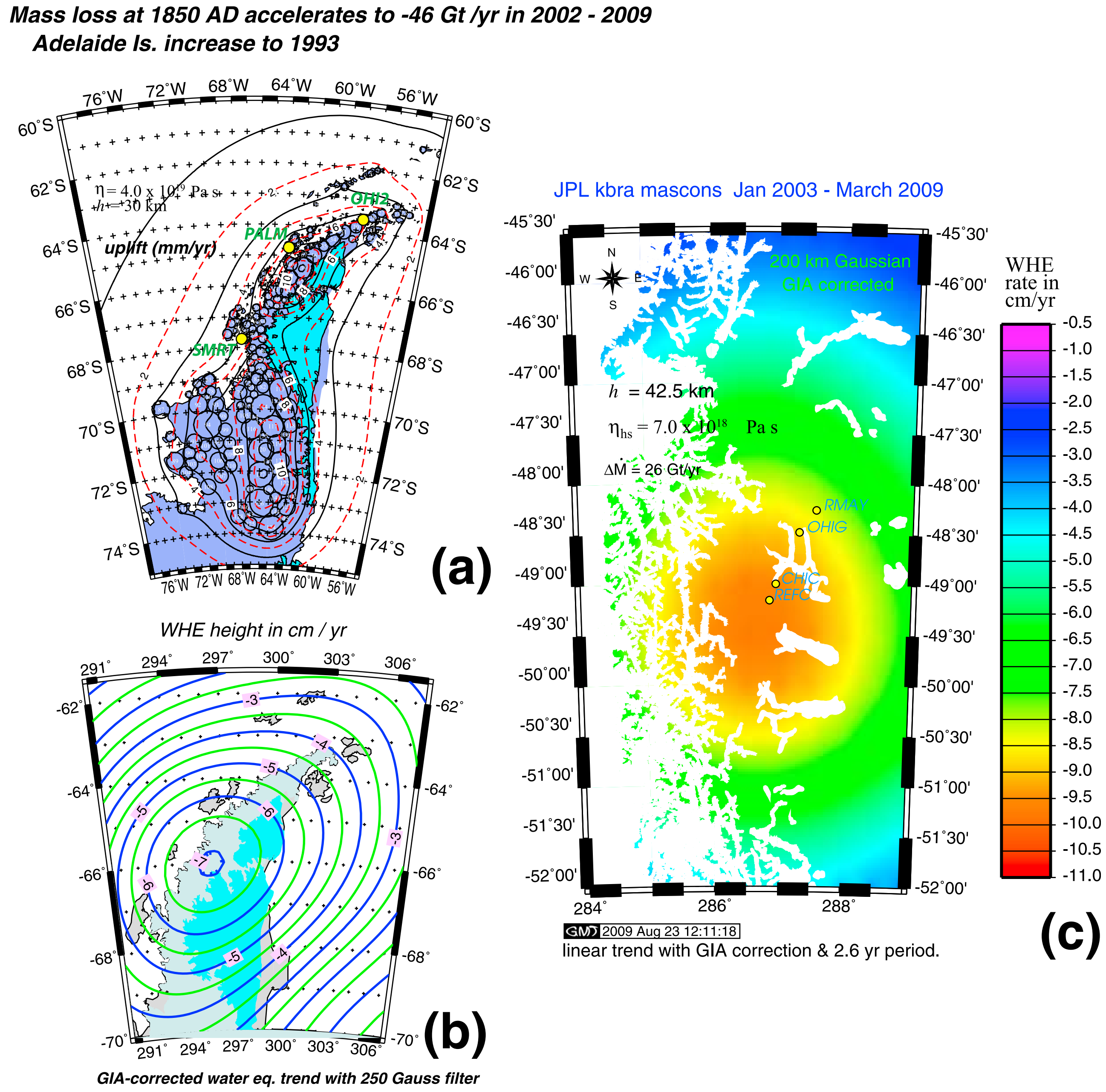

Figure 11. (a) Predicted uplift rate for the peninsula after about 50 forward model iterations. The ice model is very close to model II shown in Figure 6. (b) The 250 km Gauss-smoothed and GIA-corrected WHE. Slightly improved fits to both GRACE and GPS data were obtained with ice mass loss lowered from −46.0 to −41.5 Gt/yr in this process of optimization. (c) The GIA-corrected, 200 km Gauss-smoothed WHE rate for Patagonia.

by yellow circles. Figure 11b shows the 250 km Gauss-smoothed and GIA-corrected WHE rate for this case, and provides a reasonable explanation of both GPS and GRACE data. Figure 11c shows the GIA-corrected, 200 km Gauss-smoothed WHE rate for Patagonia. In other words, this is the GIA-corrected WHE map for the GRACE mascon trend solution, after search and removal of the amplitudes and phases of annual, semiannual, tidal alias terms S_2, K_2, a constant offset and a search for parameter centered about an oscillation of 2.6 years. The uplift is constrained by the data described by *Dietrich et al.* [2010] for SPI+NPI. One successful uplift map view is shown in Figure 12. For the computation in Figure 12, the ice model assumed $\Delta\dot{M} = -30.5$ Gt/yr.

[36] In Figure 13a the GIA-corrected, 200 km Gauss-smoothed WHE rate for Patagonia is shown using the assumption of $\Delta\dot{M} = -26$ Gt/yr. Note the contrast with the map view of Patagonian ice loss on rigid Earth in Figure 13b. Here an equivalent smoothing and truncation at degree and order $L = M = 120$ is assumed. The rigid Earth representation naturally differs from the explicit GIA-corrected WHE solution of equivalent smoothing and truncation. This occurs because GIA corrections are unintended, though necessary,

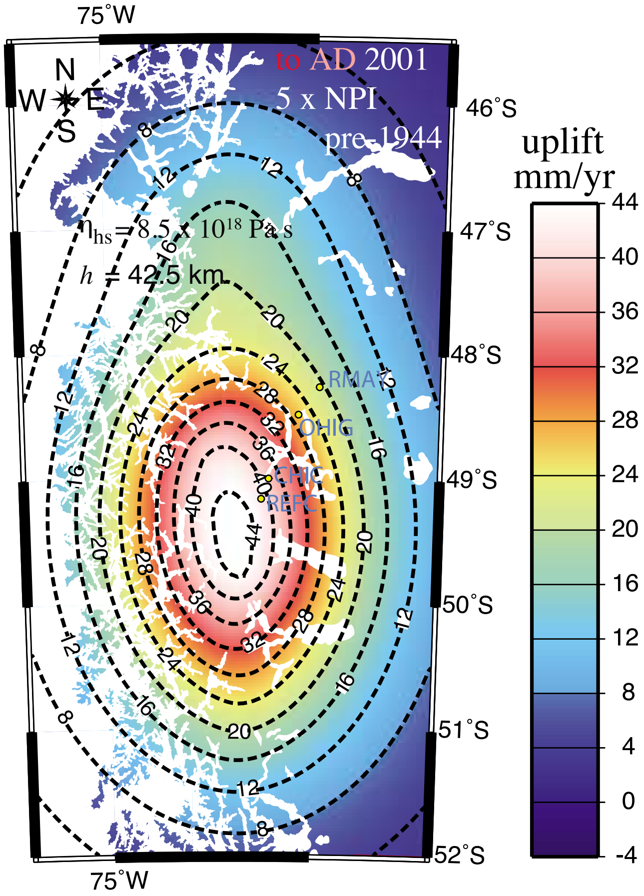

Figure 12. Map view of the predicted NPI+SPI uplift rates with the GPS stations array locations. The Patagonian GPS data and models are published by *Dietrich et al.* [2010]. The value of mantle viscosity, lithospheric thickness, and present-day ice mass loss (−30.5 Gt/yr) corresponds to one of nearly 50 iterations to deliver the optimization of GPS-GRACE data combination. A slightly better fit was found with 2003–2009 losses at −26.6 Gt/yr.

forms of smoothing. Slow isostatic viscous deformation processes in the solid Earth are of longer wavelength than are the surface loads that drive them. The GIA correction has longer wavelengths, therefore, that cannot be suppressed. Note also that peak amplitudes differ by ~10%. The differences should highlight a cautionary note when GIA modelers deliver WHE "corrections" to the hydrology community.

[37] For the Antarctic Peninsula, GIA corrections south of the SMRT GPS station (Table 1 and maps in Figures 1 and 2) are uncertain and contribute more to the total mass loss error budget (±9 Gt/yr) than other factors. The uncertainty south of SMRT also stems from the paucity of dated glaciogeomorphological constraints younger than about 7.2 kyr B.P. [*Bentley et al.*, 2006], and evidence for crustal rebound from Last Glacial Maximum dates to this part of the Holocene [*Roberts et al.*, 2009].

5.5. Optimization

[38] In the northern hemisphere, where GIA models are better constrained and continuous GPS tracking stations are numerous, it is possible to make more formal and sophisticated simultaneous inversions for Earth parameters and ice models [e.g., *Hill et al.*, 2010; *Wu et al.*, 2010]. The method we have employed here is far less rigorous, for example, than that of *Rangelova and Sideris* [2008], who formally introduce methods for combining terrestrial gravity and crustal motion data with GRACE data. However, all of the iterative steps employed here are rooted in an analogous optimization concept.

[39] For any region having (1) coeval GPS vertical time series and (2) a computable GIA correction that is constrained by independent data, and coeval space gravimetry data for determining $\dot{\bar{C}}^{S}_{\ell mj}$, a formal statement can be written for the optimization problem for determining ice mass changes by combining secular GPS uplift and space gravimetry data. Retaining the ice-to-ocean mass conservation in the harmonic domain (see equation (3)) and ignoring error propagation,

$$\frac{3\rho_{\rm ice}}{(2\ell+1)\bar{\rho}_e R_E}\left[\sum_{i=1}^{\mathcal{I}_{\rm disk}}\tilde{w}_{\ell mj,i}\dot{D}_i^{(P)}-\frac{\rho_{\rm w}}{\rho_{\rm ice}(2\ell+1)}\dot{\xi}\bar{a}_{\ell mj}\right]-\left[\dot{\bar{C}}^{S}_{\ell mj}-\dot{\bar{C}}^{\rm GIA}_{\ell mj}\right]=0. \tag{13}$$

For fully self-consistent disc height change forward models of the GRACE plus GPS data, with all time terms, p, accounted for in computing $\dot{\bar{C}}^{\rm GIA}_{\ell mj}$, the terms in brackets should exactly balance one another. The first term enclosed by brackets is the effective rigid Earth normed Stokes coefficients for the mass transport, whereas the second term in brackets is the observed GRACE minus GPS corrected Stokes coefficients. Ideally, the two terms in brackets are identical. The iterations in this paper strive toward equivalence of the two terms. The left-hand side of equation (13) may be regarded as a functional $\mathcal{E}$. It is to be understood that an additional requirement is a minimization of the difference between predicted and observed vertical velocity at stations (θ_k, λ_k);

$$\mathcal{F}\equiv\dot{u}^{r^{GIA}}(\theta_k,\lambda_k)-\dot{u}^{r^{GPS}}(\theta_k,\lambda_k)=0, \tag{14}$$

using the identical GIA computation for $\dot{\bar{C}}^{\rm GIA}_{\ell mj}$. The minimizations of $\mathcal{E}$ and $\mathcal{F}$ then form the mathematical statement of the optimization problem. Our model "best fit" to the GPS data is given in Table 1. The path to optimization is analogous to previously proposed uses of GRACE-ICESat data combination for simultaneous solution of Antarctic GIA and ice mass balance [*Wahr et al.*, 2000; *Wu et al.*, 2002]. This combination method is now partially realized, but the best solutions are far from either the Antarctic Peninsula or the Patagonia Ice Fields [*Riva et al.*, 2009].

5.6. Rigid Earth Water Height

[40] The GIA-corrected WHE trend is, essentially, the solution for ice mass trend sought by glacial hydrologists during the GRACE observing period. If that ice loss, however, were to be recomputed on a rigid Earth it would predict a somewhat different pattern (see Figure 13), due to the fact that the GIA correction always samples mass changes outside of the target region. However, the discrepancies are at, or below, the ±1 cm/yr level, which is near the floor level of our errors for the mascon analysis, which we find to be near ±0.5 cm/yr at this latitude.

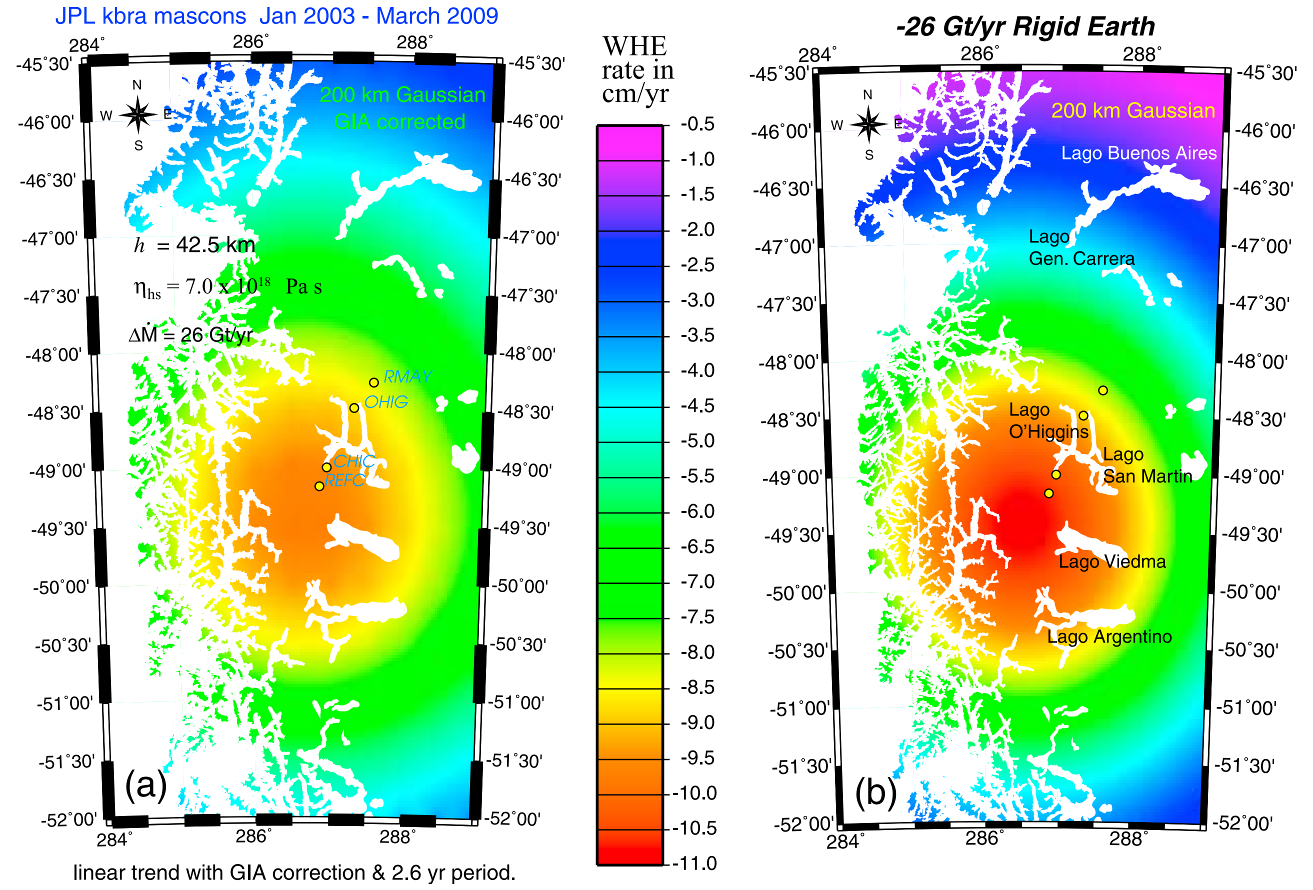

Figure 13. (a) Map view of GIA-corrected, 200 km Gauss-smoothed WHE rate for Patagonia using the solution $\Delta\dot{M} = -26$ Gt/yr. The Patagonian SCE distribution corresponds to that of Table S1 of *Dietrich et al.* [2010]. (b) The same Patagonian ice loss but represented on a rigid Earth. Mantle-lithosphere parameters are as indicated in labels in Figure 13a. The rigid Earth representation naturally differs from the explicit GIA-corrected WHE solution of equivalent smoothing and truncation as the correction has longer wavelengths that cannot be suppressed.

5.7. Predicted Water Heights and Altimetry

[41] As gravity and ice sheet height change observations constraining $\dot{D}_i^{(P)}$ are measured independently, a comparison of the first and second terms in brackets of equation (13) provide a measure of the success of formally removing the GIA part of the trend using simultaneous satellite measurement of gravity and altimetry. In Figure 14 we use the corresponding sum to degree and order 1900 for mapping $\dot{h}$, a computation requiring Clenshaw summation techniques at the latitudes of the AP [*Holmes and Featherstone*, 2002]. The SH representation truncated at 1900 serves as smoothing filter using the uppermost wavelength limits of the SCE representation. This map may be compared to altimetry measurements for the firn compaction-corrected ice height trends. The ICESat altimetric height differences between 2003 and 2007 record substantial lowering of uncorrected surface topography [*Pritchard et al.*, 2009] located near the on-land snouts of the outlet glaciers. The height changes predicted in Figure 14 are roughly in accord with the magnitude and spatial pattern recovered in the combined GRACE-GPS small cap ensemble. Note that the predicted heights are from equation (11) using equations (10) and (12) to construct the coefficients in the SH expansion.

[42] The individual ICESat tracks that can be used for height changes in the Antarctic Peninsula are relatively sparse. A high-quality near-repeat track from *Pritchard et al.* [2009] is shown in Figure 15a. Although errors are dependent upon topographic slope, the interpolation method of *Pritchard et al.* [2009] yields 1σ errors in detection of ice height change at the level ±7 cm/yr. While our model error has not been formally estimated as propagated from the covariance matrix of the GLM, we estimate it to be at least about ±20 cm/yr at the location of the peaks in box B of Figure 14. Using the pixels that record height changes across the track shown, we derive an average height loss of −98 ± 11 cm/yr water equivalent. Here we adjust altimetry height trends by the ratio ρ_f/ρ_w using a firn density, ρ_f value from *van den Broeke* [2008] of 0.55 Gt/km^3. At the location of the boxed region in Figure 14 (box A) the comparison reveals that our GRACE-GPS based solution predicts WHE rates of about −40 to −60 cm/yr versus ICESat average along the track of −98 cm/yr. Note the lowering by a rate of over 100 cm/yr in the northern BP near the largest negative values

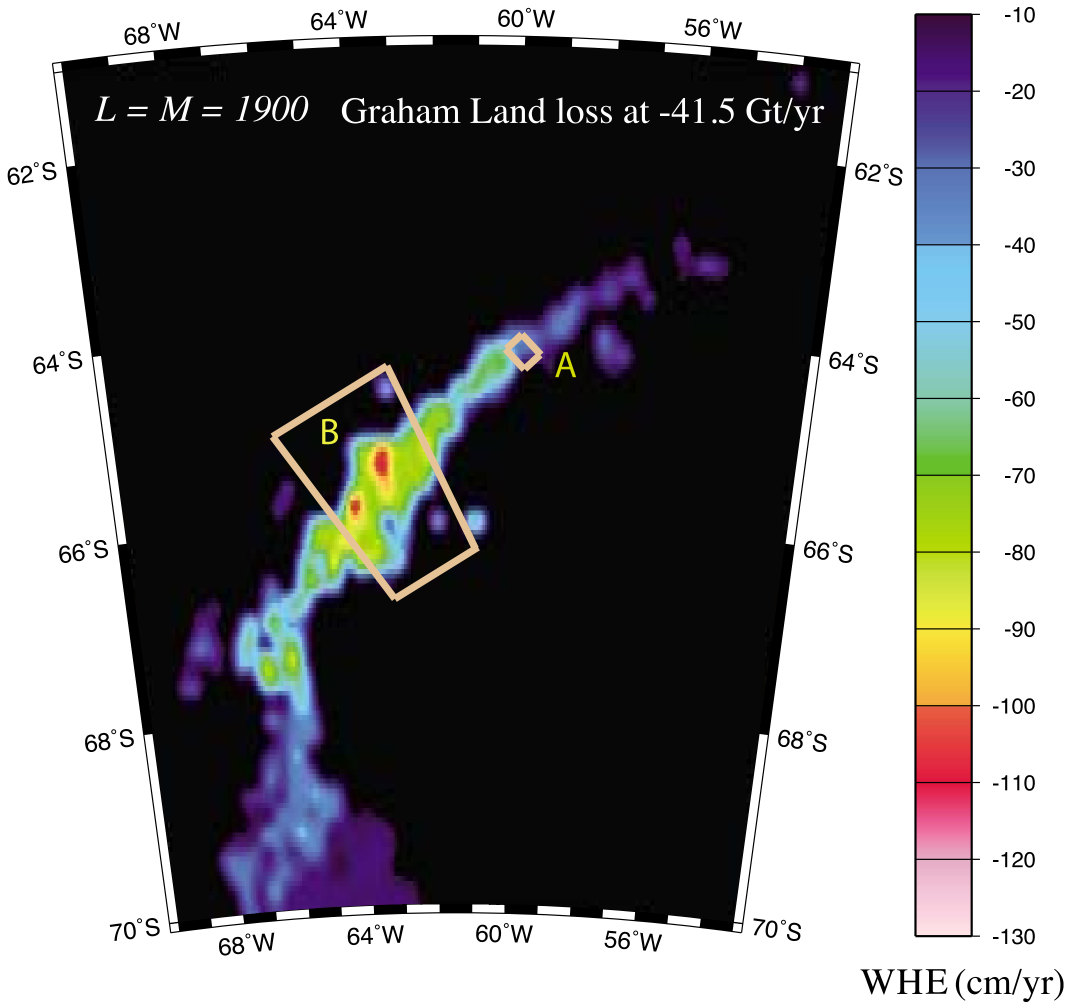

Figure 14. Water height change ($\dot{h}$ predicted for the final iterated Antarctic Peninsula model. The starting ice model was model II. GIA-corrected GRACE mascon solution for present-day ice loss in WHE resolved to $\Delta\lambda \approx 10.5$ km. The SH expansion is truncated at degree and order 1900. The hot colors peak in the BP. The map is not constructed from the SCE height rates $\dot{D}_i^{(P)}$ of equations (3) and (13) but rather of equations (11) and (12) with no Gaussian filtering: $W_\ell(\lambda_G) \rightarrow 1$.

in Figure 14. In this region, the same method is applied to Figure 15b (from near-repeat track analysis of *Pritchard et al.* [2009]) to estimate water equivalent height changes of −50 ± 11 cm/yr. An average over the box B of Figure 14 yields −75 ± 13 cm/yr. Here the averaging is over our GRACE-GPS based SCE solution for all values exceeding the amplitude of 10 cm/yr. While the comparison is very crude, it establishes a self-consistency check on the ability of our GRACE-GPS data combination method to realistically infer the amplitude of interannual trends in ice heights. Note that while the SCE solution isolates a peak negative gravity trend and ice height loss at this locale (inset B), it is smoothed, via the SH representation of equation (11), across the entire width of the Antarctic Peninsula. The SCE solutions cannot provide accurate inferences as to the locations of ice height changes.

5.8. Caveats: Implementation of Aliasing Fields and Orbit Filtering Methods

[43] A number of discrepancies remain between the different analyses centers (JPL, GFZ, CSR, DEOS, UTIG and CNES) for the recovery of reliable regional trends, often maintaining differences at a 20–30% level, even reaching 100% in important regions like Greenland [e.g., *Steffen et al.*, 2009]. The precise origin of these differences is still under investigation, and is geographically inhomogeneous. The JPL mascon solutions have in common many of the same level 2 processing steps (implementation of dealiasing fields [e.g., see *Watkins and Yuan*, 2007]) and orbit filtering procedures as in the SH release JPL RL04. A study pertinent to this general issue was performed by *Sasgen et al.* [2007].

[44] Using a Wiener filtering method that limited degree and order considerations to $12 \leq l, m \leq 50$, *Sasgen et al.* [2007] examined SH fields from JPL-RL04, CNES-RL01C, CSR-RL04, and GFZ-RL04 for the period January 2003 through December 2006 for southern latitudes higher than 60°S. For the Antarctic Peninsula region, secular trends for JPL and CNES solutions were −24.6 ± 6 Gt/yr and −31.4 ± 3 Gt/yr, representing the minimum and maximum among centers. The value of comparing these solutions and their errors is limited by the fact that full covariance analysis, with consideration of leakage, suggest 8 times larger errors [*Horwath and*

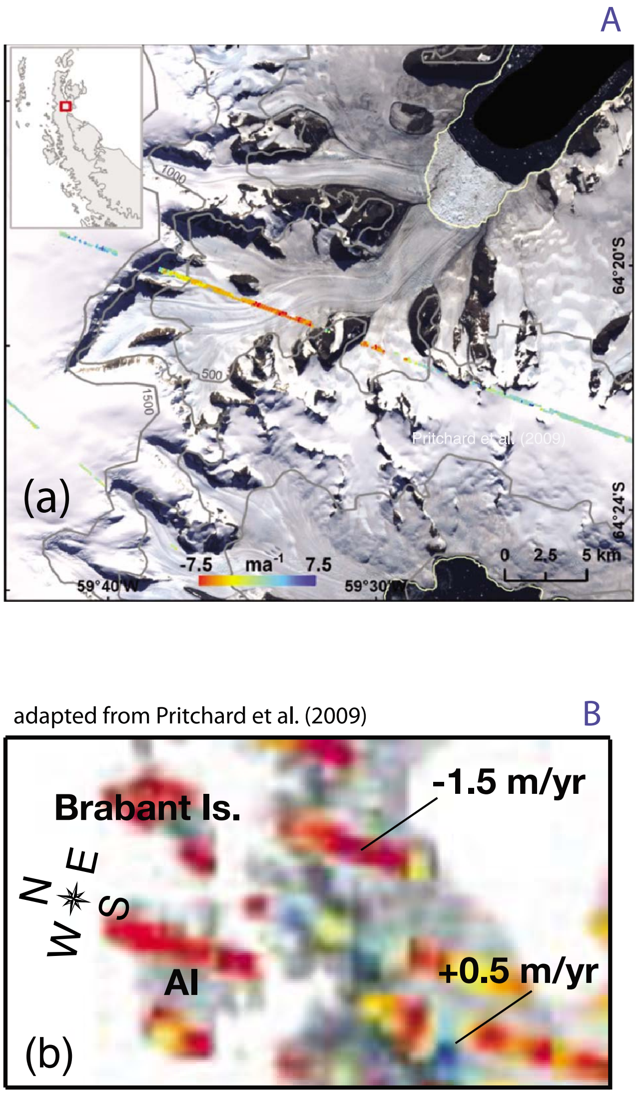

adapted from Pritchard et al. (2009)

Figure 15. Ice height trends measured by ICESat during 2003–2007 from *Pritchard et al.* [2009]. The inset regions (a) A and (b) B correspond to the like-labeled regions of Figure 14. The heights must be corrected for density to obtain WHE rates for the purpose of comparison. The peak height rates in Figure 15b are indicated. AI is Anvers Island (see Figure 1).

Dietrich, 2009] and that the CNES solutions are formed from 10 day solutions and are, hence, prone to larger uncertainties at the required high L, M truncation values for the Antarctic Peninsula. Nonetheless, these differences indicate 25% discrepencies simply due to the differences among the released SH Level 2 data in the high latitude Southern Hemisphere ($90° - \theta_k \leq -45°$). However, to date, no other GRACE analyses compete with the GLM technique used in this paper, and hence, such analysis of center dependence cannot be quantified.

6. Summary

6.1. GRACE-GPS Constrained GIA

[45] The mantle and lithosphere of Southern Patagonia and the Antarctic Peninsula lie in the tectonic wake of geologically youthful triple junction migrations. This is the setting of the solid Earth models for the isostatic response fields studied in this paper. The ice masses of GL and the SPI+NPI roof crust that has seen recent upwelling of volatile-rich mantle material that has invaded a slab window environment, where hot ocean ridges were subducted during the last 3–12 Myr [e.g., *Ivins and James*, 1999; *Vuan et al.*, 2005; *Klemann et al.*, 2007; *Groome and Thorkelson*, 2009]. Thus, here the mantle is likely to be of greatly reduced creep strength and effective viscosity. This reduction increases the sensitivity of predicted GIA to the last 250 years of ice loading. Both the reduced creep strength and the spatial dimensions of the LIA ice loading-unloading restrict the responses to relatively short wavelengths as well. Here a mascon technique for GRACE data analysis delivers the required accuracy and spatial resolution. The lithosphere-mantle parameters that best satisfy the GRACE-GPS data combination are retrieved, given the assumptions of modeled LIA, and LIA to present-day ice mass changes. The bound on elastic lithosphere thicknesses are similar: $20 \leq h \leq 50$ km, but distinctly different for mantle viscosity for south Patagonia ($4–8 \times 10^{18}$ Pa s) versus the AP ($3–10 \times 10^{19}$ Pa s). For Antarctica these are the first data-based estimates of shallow upper mantle viscosity. As the number of continuous (or quasi-continuous) GPS stations increase, a revisit to the modeling should consider a finite depth (or thickness) of the asthenospheric portion of the upper mantle, as in the studies by *Larsen et al.* [2005] and *James et al.* [2009]. The region studied by *James et al.* [2009] samples mantle viscosity in a juvenile slab window environment [*Groome and Thorkelson*, 2009]. This has the potential for an interesting comparison, for the retrieved viscosity in the thickest asthenosphere case studied is about 4×10^{19} Pa s, quite consistent with our solved-for AP half-space values.

6.2. GRACE-GPS Constrained $\Delta\dot{M}$

[46] Our GLM solutions identify the most probable landforms that are losing extreme amounts of mass, specifically the BP, and their immediate surrounding outlet glaciers, and the center north of the SPI (seen in Figure 1). In Figure 14 the SCE solution for WHE rate is shown with SH expansion to 1900. The distribution of mass loss among individual SCE members is uncertain. Tests with the GPS data indicate that the caps may exchange height trend with any nearest neighbor and negligibly affect the optimization. In fact, the study with the three models of Figures 5–10 indicate that climatic regions removed by several hundred km from the southernmost GPS tracking station (see Figure 2) are poorly constrained by the uplift data.

[47] The negative height changes of 1–2 m/yr retrieved using airborne and ICESat cross tracks in 2002 [*Rignot et al.*, 2005], and those from 7 year ICESat repeat tracks, which are of order −1 to −10 m/yr [*Pritchard et al.*, 2009], indicate that the GLM-GPS small cap ensemble predict quite reasonable average height trends without altimetry data. While this result should be confirmed with more comprehensive altimetry data sets, it does eliminate the possibility that increased BP snow accumulation [e.g., *Thomas et al.*, 2008] is a significant counterbalance to loss by ice stream flux during the period 2003–2009. The GPS bedrock uplift data provide critical control for stabilizing the mass balance estimate and the ice height change predictions.

Table 4. Peninsula Net Imbalance Estimates (Gt/yr)[a]

Study Date	Graham Land (GL)	Antarctic Peninsula
1996 A	−5 ± 6	−13 ± 23
1996 A^+	−12 ± 7	−25 ± 45
2000 A	−5 ± 6	−13 ± 23
2000 A^+	−15 ± 8	−28 ± 45
2005 A^+	- - -	−57 ± 21
2006 A	−34 ± 6	−42 ± 24
2006 A^+	−47 ± 9	−60 ± 46
2003–2009.25 GLM	−32 ± 6	−41.5 ± 9

[a] All values from *Rignot et al.* [2008] except 2005 A^+ [*Pritchard and Vaughan*, 2007] and 2003–2009.25 GLM (this study).

[48] Finally, it is of note that a recent forward model analysis of a CSR-RL04 2002–2009 time series by *Chen et al.* [2009] for the Antarctic Peninsula estimated a GIA-corrected secular loss rate of −35.5 Gt/yr, using the IJ05 GIA model of *Ivins and James* [2005]. Differences between IJ05 and the GPS-enhanced recomputation of GIA here suggest errors of about 13 Gt/yr for the later secular mass trend. The new GIA-corrected trend for the Antarctic Peninsula (see the entire boxed region of Figure 1) that is revealed with the higher resolution GLM technique is −41.5 ± 9 Gt/yr, with 85% of the signal isolated to GL (Figure 14), with errors dominated by residual GIA model ambiguities, and a small fractional errors from intrinsic GRACE mascon reduction of ranging signal and GPS uplift trends. The new estimate is also comparable to the flux/accumulation estimates of *Rignot et al.* [2008] for 2006, for surveyed areas (without area extrapolation [see *Rignot et al.*, 2008, Tables 1 and 2]), as these are −34 ± 6 Gt/yr for GL and −8 ± 18 Gt/yr for the remainder of the Antarctic Peninsula. Our newly estimated mass budget trends over 2003–2009.3 are −35.3 ± 7.6 Gt/yr for GL and −6.2 ± 1.4 Gt/yr for the remainder of the Antarctic Peninsula, and are entirely within one σ of the area-extrapolated 2006 estimate of *Rignot et al.* [2008] for the same regions. The estimates for Peninsula $\Delta\dot{M}$ reported by *Rignot et al.* [2008] and *Pritchard and Vaughan* [2007] are summarized in Table 4 alongside our new GLM result. The inference of substantial acceleration since the mid-1990s though the early 2000s is clear. Our result, however, suggests a flattening off of this acceleration during the mid-2000s to a relatively constant loss rate. Note that new 2003–2009.25 GLM mass imbalance result is just within 1σ of the area-measured (A) and the area-plus-extrapolated (A^+) results for 2006 reported by *Rignot et al.* [2008], for GL and well within the 1σ results for the entire Peninsula. In other words, we have found no evidence for further acceleration above that determined for 1996 to 2006.

6.3. GRACE-GPS Constrained $\Delta\dot{M}$: Southernmost Patagonia

[49] *Rignot et al.* [2003] and *Dietrich et al.* [2010] found acceleration from 1995 to 2000 for the SPI. Our measurements are for 2003–2009.25 and we find a slightly reduced loss rate, well within the 1σ range of errors of the two estimates. We conclude that there has been no acceleration during the last 10 or more years. This is a new result and reveals that the region has fallen into state of steady demise at a rate of about −26 Gt/yr. While this demise might not be accelerating for the PIF, the new steadiness of the rate forebodes a very unhealthy prognosis for the future of glaciers there.

7. Conclusion

[50] Between January 2003 and March 2009 the Patagonian Ice Fields and Graham Land of the greater northern Antarctic Peninsula have lost 26 ± 6 Gt/yr and 41.5 ± 9 Gt/yr, respectively. Collectively, the contribution to rate of sea level rise from the two glacier regimes is 0.19 ± 0.045 mm. Reevaluation of ice balance in southern Patagonia [*Dietrich et al.*, 2010] for 1975–2000 suggests that our GRACE solutions and the mass balance study using topographic and areal data [*Rignot et al.*, 2003] are consistent in rate loss estimate to well within the one σ level of the error budgets. The loss rates prior to 2003 for both the AP and the SPI sustained substantial acceleration [*Vaughan et al.*, 2003; *Rignot et al.*, 2005; *Pritchard and Vaughan*, 2007; *Rignot et al.*, 2003]. We conclude that ice complexes in the heart of Graham Land and in central southern Patagonia (Figure 1) are disappearing at rates comparable to those measured during years just prior to the 2002 launch of GRACE using height and area change observations. Therefore, the new GRACE-GPS observations aid in establishing the timescale for ice loss to be an interdecadal one, both north and south of the Drake Passage. Land glaciers have evolved into a new state of sustained and stronger demise over the past 60 years, clearly following a shift in regional climate [e.g., *Thompson and Solomon*, 2002; *Vaughan et al.*, 2003; *Turner et al.*, 2005; *van Lipzig et al.*, 2008; *Mayewski et al.*, 2009]. The projection of Drake Passage climate evolution into the future, as portrayed in numerical simulation using global climate scenarios, remains uncertain [*Sen Gupta et al.*, 2009]. In fact, over the period of GRACE observation (2003–2009) sea surface temperatures in the Drake Passage have experienced a period of moderate cooling (~−0.2 to −0.4°C) [*Naveira-Garabato et al.*, 2009], suggesting that the adjacent land ice losses are controlled by much longer-term rising climatic temperature [e.g., *Marshall et al.*, 2006]. While sustained ice shelf loss could drive a plethora of possible large-scale nonlinear ice sheet and climate feedback dynamics [e.g., *Kaspi et al.*, 2004], there is no compelling evidence of such mechanisms in action during the combined GRACE and space radar observing period. It is important to add, however, that individual glacier systems, such as those that feed into the coastal waters where the Wordie Ice Shelf collapsed in 1989, indeed, continue to accelerate in their rate of mass loss [*Wendt et al.*, 2010]. The observation that mass loss in Graham Land appears not to be accelerating is somewhat of an enigma, in light of the reduced buttressing force of the Larsen B Ice Shelf in 2002. Possible explanations are that increases in loss rate only occurred just prior to the beginning of our GRACE time series, or, that increases in accumulation are counterbalancing the increases in glacier outlet fluxes during 2003–2009.25.

[51] **Acknowledgments.** This research was supported by NASA's Earth Surface and Interior Focus Area as part of the GRACE Science Team effort and was performed at the Jet Propulsion Laboratory, California Institute of Technology. Parts of this research were supported by the International Bureau of the BMBF (Germany) and by the Chilean Government through the Millennium Science Initiative and the Centers of Excellence Base Financing Program of Conicyt which fund and the Centro de Estudios Científicos (CECS). We thank Michael Bentley, David Bromwich, Ben Chao, Eugene

Domack, Tom James, Matt King, Felix Landerer, Eric Rignot, Riccardo Riva, Christopher Shuman, Alexander Simms, Xiaoping Wu, and Victor Zlotnicki for their insight and helpful comments. Many of the figures in this paper were created using GMT open software [*Wessel and Smith*, 1995].

References

Allen, C. S., L. Oakes-Fretwell, J. B. Anderson, and D. A. Hodgson (2010), A record of Holocene glacial and oceanographic variability in Neny Fjord, Antarctic Peninsula, *Holocene*, *20*, 551–564, doi:10.1177/0959683609356581.

Altamimi, Z., X. Collilieux, J. Legrand, B. Garayt, and C. Boucher (2007), ITRF2005: A new release of the International Terrestrial Reference Frame based on time series of station positions and Earth orientation parameters, *J. Geophys. Res.*, *112*, B09401, doi:10.1029/2007JB004949.

Amalvict, M., P. Willis, G. Wöppelmann, E. R. Ivins, M.-N. Bouin, L. Testut, and J. Hinderer (2009), Isostatic stability of the East Antarctic station Dumont d'Urville from long-term geodetic observations and geophysical models, *Polar Res.*, *28*, 193–202, doi:10.1111/j.1751-8369.2008.00091.x.

Barcaza, G., M. Aniya, T. Matsumoto, and T. Aoki (2009), Satellite-derived equilibrium lines in Northern Patagonia Icefield, Chile, and their implications to glacier variations, *Arct. Antarct. Alp. Res.*, *41*, 174–182, doi:10.1657/1938-4246-41.2.174.

Bentley, M. J., C. J. Fogwill, P. W. Kubik, and D. E. Sugden (2006), Geomorphological evidence and cosmogenic ^{10}Be/^{26}Al exposure ages for the Last Glacial Maximum and deglaciation of the Antarctic Peninsula Ice Sheet, *Geol. Soc. Am. Bull.*, *118*, 1149–1159, doi:10.1130/B25735.1.

Bentley, M. J., et al. (2009), Mechanisms of Holocene palaeoenvironmental change in the Antarctic Peninsula region, *Holocene*, *19*, 51–69, doi:10.1177/0959683608096603.

Bevis, M., et al. (2009), Geodetic measurements of vertical crustal velocity in West Antarctica and the implications for ice mass balance, *Geochem. Geophys. Geosyst.*, *10*, Q10005, doi:10.1029/2009GC002642.

Braun, M., A. Humbert, and A. Moll (2009), Changes of Wilkins Ice Shelf over the past 15 years and inferences on its stability, *Cryosphere*, *3*, 41–56, doi:10.5194/tc-3-41-2009.

Chambers, D. P. (2006), Evaluation of new GRACE time-variable gravity data over the ocean, *Geophys. Res. Lett.*, *33*, L17603, doi:10.1029/2006GL027296.

Chao, B. F. (2005), On inversion for mass distribution from global (time-variable) gravity field, *J. Geodyn.*, *39*, 223–230, doi:10.1016/j.jog.2004.11.001.

Chen, J. L., C. R. Wilson, B. D. Tapley, D. D. Blankenship, and E. R. Ivins (2007), Patagonia icefield melting observed by gravity recovery and climate experiment (GRACE), *Geophys. Res. Lett.*, *34*, L22501, doi:10.1029/2007GL031871.

Chen, J. L., C. R. Wilson, B. D. Tapley, D. D. Blankenship, and D. Young (2008), Antarctic regional ice loss rates from GRACE, *Earth Planet. Sci. Lett.*, *266*, 140–148, doi:10.1016/j.epsl.2007.10.057.

Chen, J. L., C. R. Wilson, D. Blankenship, and B. D. Tapley (2009), Accelerated Antarctic ice loss from satellite gravity measurements, *Nat. Geosci.*, *2*, 859–862, doi:10.1038/ngeo694.

Cook, A. J., and D. G. Vaughan (2010), Overview of areal changes of the ice shelves on the Antarctic Peninsula over the past 50 years, *Cryosphere*, *4*, 77–98, doi:10.5194/tc-4-77-2010.

Dach, R., U. Hugentobler, P. Fridez, and M. Meindl (Eds.) (2007), Bernese GPS software version 5.0, Astron. Inst., Univ. of Bern, Bern, Switzerland.

Dietrich, R., E. R. Ivins, G. Casassa, H. Lange, J. Wendt, and M. Fritsche (2010), Rapid crustal uplift in Patagonia due to enhanced ice loss, *Earth Planet. Sci. Lett.*, *289*, 22–29, doi:10.1016/j.epsl.2009.10.021.

Domack, E. W., A. Leventer, R. Dunbar, F. Taylor, S. Brachfeld, and C. Sjunneskog (2001), Chronology of the Palmer Deep site, Antarctic Peninsula: A Holocene palaeoenvironmental reference for the circum-Antarctic, *Holocene*, *11*, 1–9, doi:10.1191/095968301673881493.

Domack, E. W., S. E. Ishman, A. B. Stein, C. E. McClennen, and A. J. Timothy (1995), Late Holocene advance of the Müller Ice Shelf, Antarctic Peninsula: Sedimentological, geochemical and palaeontological evidence, *Antarct. Sci.*, *7*, 159–170, doi:10.1017/S0954102095000228.

Domack, E., D. Duran, A. Leventer, S. Ishman, S. Doane, S. McCallum, D. Amblas, J. Ring, R. Gilbert, and M. Prentice (2005), Stability of the Larsen B ice shelf on the Antarctic Peninsula during the Holocene epoch, *Nature*, *436*, 681–685, doi:10.1038/nature03908.

Flechtner, F., M. Thomas, and H. Dobslaw (2010), Improved non-tidal atmospheric and oceanic de-aliasing for GRACE and SLR satellites, in *System Earth via Geodetic-Geophysical Space Techniques: Advanced Technologies in Earth Sciences, Part 2*, edited by F. Flechtner et al., pp. 131–142, Springer, Berlin, doi:10.1007/978-3-642-10228-8_11.

Groome, W. G., and D. J. Thorkelson (2009), The three-dimensional thermo-mechanical signature of ridge subduction and slab window migration, *Tectonophysics*, *464*, 70–83, doi:10.1016/j.tecto.2008.07.003.

Guinn, J., J. Jee, P. Wolff, F. Lagattuta, T. Drain, and V. Sierra (1994), TOPEX/POSEIDON operational orbit determination using global positioning satellites, *TDA Progress Rep. 42–116*, pp. 162–174, Jet Propul. Lab., Pasadena, Calif.

Hall, B. L. (2009), Holocene glacial history of Antarctica and the sub-Antarctic islands, *Quat. Sci. Rev.*, *28*, 2213–2230, doi:10.1016/j.quascirev.2009.06.011.

Hall, B. L., T. Koffman, and G. H. Denton (2010), Reduced ice extent on the western Antarctic Peninsula at 700–970 cal. yr B.P, *Geology*, *38*, 635–638, doi:10.1130/G30932.1.

Hanson, R. J., and C. L. Lawson (1969), Extensions and applications of the Householder algorithm for solving linear least squares problems, *Math. Comput.*, *23*, 787–812, doi:10.1090/S0025-5718-1969-0258258-9.

Hill, E. M., J. L. Davis, M. E. Tamisiea, and M. Lidberg (2010), Combination of geodetic observations and models for glacial isostatic adjustment fields in Fennoscandia, *J. Geophys. Res.*, *115*, B07403, doi:10.1029/2009JB006967.

Hodgson, D. A., M. J. Bentley, S. J. Roberts, J. A. Smith, D. E. Sugden, and E. W. Domack (2006), Examining Holocene stability of Antarctic Peninsula ice shelves, *Eos Trans. AGU*, *87*(31), 305, doi:10.1029/2006EO310001.

Holmes, S. A., and W. E. Featherstone (2002), A unified approach to the Clenshaw summation and the recursive computation of very high degree and order normalized associated Legendre functions, *J. Geod.*, *76*, 279–299, doi:10.1007/s00190-002-0216-2.

Horwath, M., and R. Dietrich (2009), Signal and error in mass change inferences from GRACE: The case of Antarctica, *Geophys. J. Int.*, *177*, 849–864, doi:10.1111/j.1365-246X.2009.04139.x.

Ivins, E. R., and T. S. James (1999), Simple models for late Holocene and present-day Patagonian glacier fluctuations and predictions of a geodetically detectable isostatic response, *Geophys. J. Int.*, *138*, 601–624, doi:10.1046/j.1365-246x.1999.00899.x.

Ivins, E. R., and T. S. James (2005), Antarctic glacial isostatic adjustment: A new assessment, *Antarct. Sci.*, *17*, 541–553, doi:10.1017/S0954102005002968.

Ivins, E. R., C. G. Sammis, and C. F. Yoder (1993), Deep mantle viscous structure with prior estimate and satellite constraint, *J. Geophys. Res.*, *98*, 4579–4609, doi:10.1029/92JB02728.

Ivins, E. R., C. A. Raymond, and T. S. James (2000), The influence of 5000 year-old and younger glacial mass variability on present-day crustal rebound in the Antarctic Peninsula, *Earth Planets Space*, *52*, 1023–1029.

Ivins, E. R., C. A. Raymond, and T. S. James (2002), Late-Pleistocene, Holocene and present-day ice load evolution in the Antarctic Peninsula: Models and predicted vertical crustal motion, in *Ice Sheets, Sea Level and the Dynamic Earth*, *Geodyn. Ser.*, vol. 29, edited by J. X. Mitrovica and B. Vermeersen, pp. 133–155, AGU, Washington, D. C.

James, T. S., and E. R. Ivins (1998), Predictions of Antarctic crustal motions driven by present-day ice sheet evolution and by isostatic memory of the Last Glacial Maximum, *J. Geophys. Res.*, *103*, 4993–5017, doi:10.1029/97JB03539.

James, T. S., E. J. Gowan, I. Wada, and K. Wang (2009), Viscosity of the asthenosphere from glacial isostatic adjustment and subduction dynamics at the northern Cascadia subduction zone, British Columbia, Canada, *J. Geophys. Res.*, *114*, B04405, doi:10.1029/2008JB006077.

Jones, P. D., M. New, D. E. Parker, S. Martin, and I. G. Rigor (1999), Surface air temperature and its changes over the past 150 years, *Rev. Geophys.*, *37*, 173–199, doi:10.1029/1999RG900002.

Kaspi, Y., R. Sayag, and E. Tziperman (2004), A "triple sea-ice state" mechanism for the abrupt warming and synchronous ice sheet collapses during Heinrich events, *Paleoceanography*, *19*, PA3004, doi:10.1029/2004PA001009.

Kaula, W. M. (1966), *Theory of Satellite Geodesy*, 122 pp., Blaisdell, Waltham, Mass.

Khan, S. A., J. Wahr, M. Bevis, I. Velicogna, and E. Kendrick (2010), Spread of ice mass loss into northwest Greenland observed by GRACE and GPS, *Geophys. Res. Lett.*, *37*, L06501, doi:10.1029/2010GL042460.

Klemann, V., E. R. Ivins, Z. Martinec, and D. Wolf (2007), Models of active glacial isostasy roofing warm subduction: Case of the South Patagonian Ice Field, *J. Geophys. Res.*, *112*, B09405, doi:10.1029/2006JB004818.

Lambeck, K., and A. Cazenave (1976), Long term variations in the length of day and climate change, *Geophys. J. R. Astron. Soc.*, *46*, 555–573, doi:10.1111/j.1365-246X.1976.tb01248.x.

Larsen, C. F., R. J. Motyka, J. T. Fryemueller, K. A. Echelmeyer, and E. R. Ivins (2005), Rapid viscoelastic uplift in southern Alaska caused by post-Little Ice Age retreat, *Earth Planet. Sci. Lett.*, *237*, 548–560, doi:10.1016/j.epsl.2005.06.032.

Luthcke, S. B., A. A. Arendt, D. D. Rowlands, J. J. McCarthy, and C. F. Larsen (2008), Recent glacier mass changes in the Gulf of Alaska region from GRACE mascon solutions, *J. Glaciol.*, *54*, 767–777, doi:10.3189/002214308787779933.

Marshall, G. J., A. Orr, N. P. M. van Lipzig, and J. C. King (2006), The impact of a changing Southern Hemisphere annular mode on Antarctic Peninsula summer temperatures, *J. Clim.*, *19*, 5388–5404, doi:10.1175/JCLI3844.1.

Masiokas, M. H., A. Rivera, L. E. Espizua, R. Villalba, S. Delgado, and J. C. Aravena (2009), Glacier fluctuations in extratropical South America during the past 1000 years, *Palaeogeogr. Palaeoclim. Palaeoecol.*, *281*, 242–268, doi:10.1016/j.palaeo.2009.08.006.

Mayewski, P. A., et al. (2009), State of the Antarctic and Southern Ocean climate system, *Rev. Geophys.*, *47*, RG1003, doi:10.1029/2007RG000231.

Naruse, R. (1997), Thinning and retreat of Glaciar Upsala, and an estimate of annual ablation changes in southern Patagonia, *Ann. Glaciol.*, *24*, 38–42.

Naveira-Garabato, A. C., L. Jullion, D. P. Stevens, K. J. Heywood, and B. A. King (2009), Variability of Subantarctic Mode Water and Antarctic Intermediate Water in the Drake Passage during the late-twentieth and early-twenty-first centuries, *J. Clim.*, *22*, 3661–3687.

Oerlemans, J. (2005), Extracting a climate signal from 169 glacier records, *Science*, *308*, 675–677, doi:10.1126/science.1107046.

Pasquini, A. I., K. I. Lecomte, and P. J. Depetris (2008), Climate change and recent water level variability in Patagonian proglacial lakes, Argentina, *Global Planet. Change*, *63*, 290–298, doi:10.1016/j.gloplacha.2008.07.001.

Pick, M. (1984), The gravitational effect of bodies with variable density, *Stud. Geophys. Geod.*, *28*, 381–392, doi:10.1007/BF01642991.

Pritchard, H. D., and D. G. Vaughan (2007), Widespread acceleration of tidewater glaciers on the Antarctic Peninsula, *J. Geophys. Res.*, *112*, F03S29, doi:10.1029/2006JF000597.

Pritchard, H. D., R. J. Arthern, D. G. Vaughan, and L. A. Edwards (2009), Extensive dynamic thinning on the margins of the Greenland and Antarctic ice sheets, *Nature*, *461*, 971–975, doi:10.1038/nature08471.

Pudsey, C. J., and J. Evans (2001), First survey of Antarctic sub-ice shelf sediments reveals mid-Holocene ice, *Geology*, *29*, 787–790, doi:10.1130/0091-7613(2001)029<0787:FSOASI>2.0.CO;2.

Pudsey, C. J., J. W. Murray, P. Appleby, and J. Evans (2006), Lee shelf history from petrographic and foraminiferal evidence, northeast Antarctic Peninsula, *Quat. Sci. Rev.*, *25*, 2357–2379, doi:10.1016/j.quascirev.2006.01.029.

Rangelova, E., and M. G. Sideris (2008), Contributions of terrestrial and GRACE data to the study of the secular geoid changes in North America, *J. Geodyn.*, *46*, 131–143, doi:10.1016/j.jog.2008.03.006.

Ray, R. D., and S. B. Luthcke (2006), Tide model errors and GRACE gravimetry: towards a more realistic assessment, *Geophys. J. Int.*, *167*, 1055–1059, doi:10.1111/j.1365-246X.2006.03229.x.

Rignot, E., A. Rivera, and G. Casassa (2003), Contribution of the Patagonia Icefields of South America to sea-level rise, *Science*, *302*, 434–437, doi:10.1126/science.1087393.

Rignot, E., G. Casassa, S. Gogineni, P. Kanagaratnam, W. Krabill, H. Pritchard, A. Rivera, R. Thomas, J. Turner, and D. Vaughan (2005), Recent ice loss from the Fleming and other glaciers, Wordie Bay, West Antarctic Peninsula, *Geophys. Res. Lett.*, *32*, L07502, doi:10.1029/2004GL021947.

Rignot, E., J. L. Bamber, M. R. van den Broeke, C. Davis, Y. Li, W. J. van de Berg, and E. van Meijgaard (2008), Recent Antarctic ice mass loss from radar interferometry and regional climate modelling, *Nat. Geosci.*, *1*, 106–110, doi:10.1038/ngeo102.

Riva, R. E. M., B. C. Gunter, T. J. Urban, L. L. A. Vermeersen, R. C. Lindenbergh, M. M. Helsen, J. L. Bamber, R. S. W. van de Wal, M. R. van den Broeke, and B. E. Schutz (2009), Glacial isostatic adjustment over Antarctica from combined ICESat and GRACE satellite data, *Earth Planet. Sci. Lett.*, *288*, 516–523, doi:10.1016/j.epsl.2009.10.013.

Roberts, S. J., D. A. Hodgson, M. J. Bentley, D. C. W. Sanderson, G. Milne, J. A. Smith, E. Verleyen, and A. Balbo (2009), Holocene relative sea-level change and deglaciation on Alexander Island, Antarctic Peninsula, from elevated lake deltas, *Geomorphology*, *112*, 122–134, doi:10.1016/j.geomorph.2009.05.011.

Robertson Maurice, S. D., D. A. Wiens, P. J. Shore, E. Vera, and L. M. Dorman (2003), Seismicity and tectonics of the South Shetland Islands and Bransfield Strait from a regional broadband seismograph deployment, *J. Geophys. Res.*, *108*(B10), 2461, doi:10.1029/2003JB002416.

Rott, H., W. Rack, P. Skvarca, and H. De Angeles (2002), Northern Larsen Ice Shelf, Antarctica: further retreat after collapse, *Ann. Glaciol.*, *34*, 277–282, doi:10.3189/172756402781817716.

Rülke, A. (2009), Zur Realisierung eines terrestrischen Referenzsystems in globalen und regionalen GPS-Netzen, Ph.D. dissertation, 188 pp., Tech. Univ., Dresden, Germany.

Rülke, A., R. Dietrich, M. Fritsche, M. Rothacher, and P. Steigenberger (2008), Realization of the Terrestrial Reference System by a reprocessed global GPS network, *J. Geophys. Res.*, *113*, B08403, doi:10.1029/2007JB005231.

Sabaka, T. J., D. D. Rowlands, S. B. Luthcke, and J.-P. Boy (2010), Improving global mass flux solutions from Gravity Recovery and Climate Experiment (GRACE) through forward modeling and continuous time correlation, *J. Geophys. Res.*, *115*, B11403, doi:10.1029/2010JB007533.

Sasgen, I., Z. Martinec, and K. Fleming (2007), Regional ice-mass changes and glacial-isostatic adjustment in Antarctica from GRACE, *Earth Planet. Sci. Lett.*, *264*, 391–401, doi:10.1016/j.epsl.2007.09.029.

Schrama, E. J. O., B. Wouters, and D. A. Lavallée (2007), Signal and noise in Gravity Recovery and Climate Experiment (GRACE) observed surface mass variations, *J. Geophys. Res.*, *112*, B08407, doi:10.1029/2006JB004882.

Sen Gupta, A., A. Santoso, A. S. Taschetto, C. C. Ummenhofer, J. Trevena, and M. H. England (2009), Projected changes to the Southern Hemisphere Ocean and sea ice in the IPCC AR4 climate models, *J. Clim.*, *22*, 3047–3078, doi:10.1175/2008JCLI2827.1.

Simon, K. M., T. S. James, and E. R. Ivins (2010), Ocean loading effects on the prediction of Antarctic glacial isostatic uplift and gravity rates, *J. Geod.*, *84*, 305–317, doi:10.1007/s00190-010-0368-4.

Skvarca, P., W. Rack, H. Rott and T. Ibarzábal-Donángelo (1999), Climatic trend and the retreat and disintegration of ice shelves on the Antarctic Peninsula: An overview, *Polar Res.*, *18*, 151–157, doi:10.1111/j.1751-8369.1999.tb00287.x.

Steffen, H., S. Petrovic, J. Müller, R. Schmid J. Wünsch, F. Barthelmes and J. Kusche, (2009), Significance of secular trends of mass variations determined from GRACE solutions, *J. Geodyn.*, *48*, 157–165, doi:10.1016/j.jog.2009.09.029.

Steigenberger, P., M. Rothacher, R. Dietrich, M. Fritsche, A. Rülke, and S. Vey (2006), Reprocessing of a global GPS network, *J. Geophys. Res.*, *111*, B05402, doi:10.1029/2005JB003747.

Steigenberger, P., M. Rothacher, M. Fritsche, A. Rülke, and R. Dietrich, (2009), Quality of reprocessed GPS satellite orbits, *J. Geod.*, *83*, 241–248, doi:10.1007/s00190-008-0228-7.

Sunseri, R. F. (2010), Mass concentration modeled as a spherical cap, *Tech. Memo. 343R-11-001*, 32 pp., Jet Propul. Lab., Pasadena, Calif., 10 Sept.

Swenson, S., and J. Wahr (2002), Methods for inferring regional surface-mass anomalies from Gravity Recovery and Climate Experiment (GRACE) measurements of time-variable gravity, *J. Geophys. Res.*, *107*(B9), 2193, doi:10.1029/2001JB000576.

Swenson, S., and J. Wahr (2006), Post-processing removal of correlated errors in GRACE data, *Geophys. Res. Lett.*, *33*, L08402, doi:10.1029/2005GL025285.

Tenzer, R., P. Moore, and O. Nezvabda (2007), Analytical solution of Newton's integral in terms of polar spherical coordinates, in *Dynamic Planet Monitoring and understanding a Dynamic Planet with Geodetic and Oceanographic Tools*, *IAG Symp.*, vol. 130, Part III, edited by P. Tregoning and C. Rizos, pp. 410–415, Springer, Berlin.

Thomas, E. R., G. J. Marshall, and J. R. McConnell (2008), A doubling in snow accumulation in the western Antarctic Peninsula since 1850, *Geophys. Res. Lett.*, *35*, L01706, doi:10.1029/2007GL032529.

Thomas, E. R., P. F. Dennis, T. J. Bracegirdle, and C. Franzke (2009), Ice core evidence for significant 100-year regional warming on the Antarctic Peninsula, *Geophys. Res. Lett.*, *36*, L20704, doi:10.1029/2009GL040104.

Thompson, D. W. J., and S. Solomon (2002), Interpretation of recent Southern Hemisphere climate change, *Science*, *296*, 895–899, doi:10.1126/science.1069270.

Thompson, L. G., D. A. Peel, E. Mosley-Thompson, R. Mulvaney, J. Dai, P.-N. Lin, M. E. Davis, and C. F. Raymond (1994), Climate since AD1510 on Dyer Plateau, Antarctic Peninsula: Evidence for recent climate change, *Ann. Glaciol.*, *20*, 420–426.

Tregoning, P., G. Ramillien, H. McQueen, and D. Zwartz (2009), Glacial isostatic adjustment and nonstationary signals observed by GRACE, *J. Geophys. Res.*, *114*, B06406, doi:10.1029/2008JB006161.

Turner, J., S. R. Colwell, G. J. Marshall, T. A. Lachlan-Cope, A. M. Carleton, P. D. Jones, V. Lagun, P. A. Reid, and S. Iagovkina (2005), Antarctic climate change during the last 50 years, *Int. J. Climatol.*, *25*, 279–294, doi:10.1002/joc.1130.

van den Broeke, M. (2008), Depth and density of the Antarctic firn layer, *Arct. Antarct. Alp. Res.*, *40*, 432–438, doi:10.1657/1523-0430(07-021)[BROEKE]2.0.CO;2.

van Lipzig, N. P. M., G. J. Marshall, A. Orr, and J. C. King (2008), The relationship between the Southern Hemisphere annular mode and Antarctic Peninsula summer temperatures: Analysis of a high-resolution model climatology, *J. Clim.*, *21*, 1649–1668, doi:10.1175/2007JCLI1695.1.

Vaughan, D. G., G. J. Marshall, W. M. Connolly, C. Parkinson, R. Mulvaney, D. A. Hodgeson, J. C. King, C. J. Pudsey, and J. Turner (2003), Recent rapid regional climate warming on the Antarctic Peninsula, *Clim. Change*, *60*, 243–274, doi:10.1023/A:1026021217991.

Velicogna, I., and J. Wahr (2006), Measurements of time-variable gravity show mass loss in Antarctica, *Science*, *311*, 1754–1756, doi:10.1126/science.1123785.

Vuan, A., S. D. Robertson Maurice, D. A. Wiens, and G. F. Panza (2005), Crustal and upper mantle S-wave velocity structure beneath the Bransfield Strait (West Antarctica) from regional surface wave tomography, *Tectonophysics*, *397*, 241–259, doi:10.1016/j.tecto.2004.12.011.

Wahr, J., M. Molenaar, and F. Bryan (1998), Time-variability of the Earth's gravity field: Hydrological and oceanic effects and their possible detection using GRACE, *J. Geophys. Res.*, *103*, 30,205–30,229, doi:10.1029/98JB02844.

Wahr, J., D. Wingham, and C. R. Bentley (2000), A method of combining ICESAT and GRACE satellite data to constrain Antarctic mass balance, *J. Geophys. Res.*, *105*, 16,279–16,294, doi:10.1029/2000JB900113.

Watkins, M., and D.-N. Yuan (2007), JPL level-2 processing standards document for level-2 product release 04, *GRACE JPL L-2 Proc Stand. Doc. RL 04 GRACE 327–744*, version 4.0, Jet Propul. Lab., Pasadena, Calif.

Wendt, J., A. Rivera, A. Wendt, F. Bown, R. Zamora, G. Casassa, and C. Bravo (2010), Recent ice-surface-elevation changes of Fleming Glacier in response to the removal of the Wordie Ice Shelf, Antarctic Peninsula, *Ann. Glaciol.*, *51*, 97–102, doi:10.3189/172756410791392727.

Wessel, P., and W. H. F. Smith (1995), New version of the generic mapping tools released, *Eos Trans. AGU*, *76*(33), 329, doi:10.1029/95EO00198.

Wu, X., M. M. Watkins, E. R. Ivins, R. Kwok, P. Wang, and J. M. Wahr (2002), Toward global inverse solutions for current and past ice mass variations: Contribution of secular satellite gravity and topography change measurements, *J. Geophys. Res.*, *107*(B11), 2291, doi:10.1029/2001JB000543.

Wu, X., M. B. Heflin, H. Schotman, B. L. A. Vermeersen, D. Dong, R. S. Gross, E. R. Ivins, A. W. Moore, and S. E. Owen (2010), Simultaneous estimation of global present-day water transport and glacial isostatic adjustment, *Nat. Geosci.*, *3*, 642–646, doi:10.1038/ngeo938.

G. Casassa, Centro de Estudios Científicos, Arturo Prat 514, Valdivia, Chile.

R. Dietrich, Institut für Planetare Geodäsie, Technische Universität Dresden, D-01069 Dresden, Germany.

E. R. Ivins, M. M. Watkins, and D.-N. Yuan, Oceans, Climate and Solid Earth Section, JPL/Caltech, Mail Stop 300-233, 4800 Oak Grove Dr., Pasadena, CA 91109-8099, USA. (erik.r.ivins@jpl.nasa.gov)

A. Rülke, Bundesamt für Kartographie und Geodäsie, Karl-Rothe-Straße 10-14, D-04105 Leipzig, Germany.